

UC San Diego

Research Theses and Dissertations

Title

Hess Deep Rift Valley Structure from Seismic Tomography

Permalink

<https://escholarship.org/uc/item/22d1s7np>

Author

Wiggins, Sean M.

Publication Date

1995

Peer reviewed

INFORMATION TO USERS

This manuscript has been reproduced from the microfilm master. UMI films the text directly from the original or copy submitted. Thus, some thesis and dissertation copies are in typewriter face, while others may be from any type of computer printer.

The quality of this reproduction is dependent upon the quality of the copy submitted. Broken or indistinct print, colored or poor quality illustrations and photographs, print bleedthrough, substandard margins, and improper alignment can adversely affect reproduction.

In the unlikely event that the author did not send UMI a complete manuscript and there are missing pages, these will be noted. Also, if unauthorized copyright material had to be removed, a note will indicate the deletion.

Oversize materials (e.g., maps, drawings, charts) are reproduced by sectioning the original, beginning at the upper left-hand corner and continuing from left to right in equal sections with small overlaps. Each original is also photographed in one exposure and is included in reduced form at the back of the book.

Photographs included in the original manuscript have been reproduced xerographically in this copy. Higher quality 6" x 9" black and white photographic prints are available for any photographs or illustrations appearing in this copy for an additional charge. Contact UMI directly to order.

UMI

A Bell & Howell Information Company
300 North Zeeb Road, Ann Arbor, MI 48106-1346 USA
313/761-4700 800/521-0600

UNIVERSITY OF CALIFORNIA, SAN DIEGO

Hess Deep Rift Valley Structure from Seismic Tomography

A dissertation submitted in partial satisfaction of the

requirements for the degree Doctor of Philosophy

in Oceanography

by

Sean Martin Wiggins

Committee in charge:

LeRoy M. Dorman, Co-chairperson
John A. Hildebrand, Co-chairperson
Peter F. Lonsdale
T. Guy Masters
John M. Goodkind
Bruce D. Cornuelle

1995

UMI Number: 9611103

UMI Microform 9611103

Copyright 1996, by UMI Company. All rights reserved.

**This microform edition is protected against unauthorized
copying under Title 17, United States Code.**

UMI

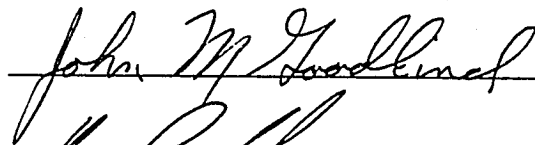
**300 North Zeeb Road
Ann Arbor, MI 48103**


Copyright

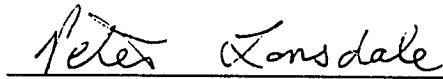
Sean Martin Wiggins, 1995


All rights reserved.

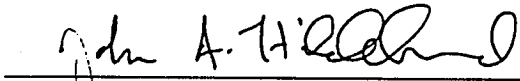
The dissertation of Sean Martin Wiggins is approved, and it is acceptable in quality and form for publication on microfilm:














Co-chairperson

Co-chairperson

University of California, San Diego

1995

iii

To the women in my life:
my daughter, to whom I have given life,
my wife, who shares my life, and
my mother, who gave me life.

"What A Long Strange Trip This Has Been"

-Robert Hunter

Table of Contents

| | |
|--------------------------------------------------------------------|------|
| Signature Page | iii |
| Dedication | iv |
| Epigraph | v |
| Table of Contents | vi |
| List of Figures | viii |
| Acknowledgements | x |
| Vita, Publications and Fields of Study | xi |
| Abstract | xii |
| 1 Geologic Background | |
| 1.1 Introduction | 1 |
| 1.2 Regional Setting: Hess Deep | 2 |
| 1.3 Petrology | 7 |
| 1.4 Ocean Drilling Program | 10 |
| 1.5 Geophysics | 10 |
| 2 Seismic Refraction Tomography Experiment at the Hess Deep | |
| 2.1 Introduction | 12 |
| 2.2 Receivers | 12 |
| 2.3 Sources | 13 |
| 2.4 Experimental Layout | 14 |
| 2.5 Source/Receiver Navigation | 16 |
| 2.6 Data | 17 |
| 3 Data Processing Techniques | |
| 3.1 Introduction | 21 |
| 3.2 Starting Model | 24 |
| 3.3 Ray Tracing | 26 |
| 3.4 Parameterization | 26 |
| 3.5 Forward Problem Matrix Calculation | 30 |
| 3.6 Inverse Procedure | 32 |
| 3.7 Synthetic Example | 34 |

| | | |
|-----|----------------------------------------------------------------------------------|----|
| 4 | Results and Discussion | |
| 4.1 | Introduction | 46 |
| 4.2 | Iterative Stopping Point | 46 |
| 4.3 | Hess Deep Velocity Model | 53 |
| 4.4 | Structural Interpretation | 60 |
| 4.5 | Conclusion | 75 |
| 5 | Topography can limit the useful range of Linearization in Tomographic Inversions | |
| 5.1 | Abstract | 76 |
| 5.2 | Introduction | 76 |
| 5.3 | Flat Laterally Homogeneous Earth | 82 |
| 5.4 | Sinusoidal Topography Earth Model | 89 |
| 5.5 | Conclusion | 94 |
| | REFERENCES | 96 |

List of Figures

Chapter 1

| | | |
|-----|-------------------------------------------------------------------------|---|
| 1.1 | Originally conceived RRR triple junction in eastern Pacific | 4 |
| 1.2 | Galapagos micro plate and its surroundings | 5 |
| 1.3 | Bathymetry of the Hess Deep rift valley | 6 |
| 1.4 | Petrological observations of the Hess Deep region - plan view | 8 |
| 1.5 | Petrological observations of the Hess Deep region - cross-section | 9 |

Chapter 2

| | | |
|-----|-------------------------------------------------------------|----|
| 2.1 | Source and receiver locations on Hess Deep bathymetry | 15 |
| 2.2 | OBS 4, west line record section | 19 |
| 2.3 | OBS 4, west line record section - reduced time | 20 |

Chapter 3

| | | |
|-----|------------------------------------------------------------|----|
| 3.1 | Flow chart of data processing method | 23 |
| 3.2 | 1-D velocity profiles | 25 |
| 3.3 | Vertical triangle functions used in parameterization | 29 |
| 3.4 | Reference model and ray paths | 38 |
| 3.5 | Intruded low velocity perturbation | 40 |
| 3.6 | Inverse results from noise-free data | 42 |
| 3.7 | Noise vs range of ray turning point | 43 |
| 3.8 | Inverse results from noisy data | 45 |

Chapter 4

| | | |
|-----|---------------------------------------------------------------------------|----|
| 4.1 | Trade-off between weighted data residuals and weighted model length | 50 |
| 4.2 | Weighted model length and weighted data residuals vs iteration | 51 |

| | | |
|------|------------------------------------------------------------------------------------|----|
| 4.3 | Travel time data residual distribution | 52 |
| 4.4 | Iterative damped least-squares inverse results | 57 |
| 4.5 | Comparison of inverse results | 59 |
| 4.6 | Sketchs of geological structural models from <i>Francheteau et al.</i> , [1990] .. | 62 |
| 4.7 | High-angle normal fault model inferred from velocity perturbation | 68 |
| 4.8 | Proposed evolution of the high-angle normal fault model | 69 |
| 4.9 | Low-angle detachment fault model inferred from velocity perturbation | 73 |
| 4.10 | Proposed evolution of the low-angle detachment fault model | 74 |

Chapter 5

| | | |
|-----|--------------------------------------------------------------------------|----|
| 5.1 | Hess Deep layered model with ray path changes | 81 |
| 5.2 | Analytical computations from equations (5.1) and (5.2) for dz/dv | 86 |
| 5.3 | Analytical computations from equations (5.1) and (5.2) for dv/dz | 87 |
| 5.4 | Ray paths traced through constant velocity gradient, flat Earths | 88 |
| 5.5 | Sinusoidal topography model with ray paths | 91 |
| 5.6 | Data/model relationship plots for sinusoidal topography model | 93 |

Acknowledgements

This dissertation represents the completion of my third project in seven years at Scripps Institution of Oceanography. I am deeply grateful for the opportunity given by my advisors, LeRoy Dorman and John Hildebrand, to conduct research on this project; finalizing my graduate career. Their scientific foresight and wisdom have been instrumental to the success of my research. I greatly appreciate the guidance and advice provided by the other members of my committee: Bruce Cornuelle, Peter Lonsdale, Guy Masters, and John Goodkind. Discussion and reviews by Chris Bradley and Mark McDonald were of great help in bouncing ideas around and exploring "what if's". Much thanks also goes to Allan Sauter for his contributions to the OBS system and Tony Schreiner for much of the processing and display software. Special thanks to Bruce Cornuelle for his patience and instruction during the implementation and running of his tomography code. I would also like to thank Captain A. Aresenault, the R/V *Thomas Washington's* crew, and resident technician John Boaz for their support during the ENCORE cruise. Finally, an infinite amount of thanks goes to Traci Wiggins for the strength and support she gave me during the past several years. This work was supported by the National Science Foundation under grant OCE-9103919.

VITA

| | |
|--------------|------------------------------------------------------------------------------------------------|
| May 15, 1965 | Born, Burbank, California |
| 1988 | B.S., Mechanical Engineering, University of California, San Diego |
| 1989-1995 | Research Assistant, Scripps Institution of Oceanography University of California, San Diego |
| 1989-1990 | California Sea Grant Fellowship |
| 1990 | M.S., Engineering Sciences, University of California, San Diego |
| 1995 | Ph.D., Oceanography, University of California, San Diego |

PUBLICATIONS

- Wiggins, Sean M., Dorman, LeRoy M., and Cornuelle, Bruce D., Linearization Limitations of Tomographic Inversion Due to Topography, *EOS*, V 75, p. 444, 1994.
- Wiggins, Sean M., Canuteson Eric L., Dorman, LeRoy M., Hildebrand, John A., Cornuelle, Bruce D., Sauter, Allan W., and Schreiner, Anthony E., Crustal Structure at the Hess Deep: Seismic Studies Show High Velocity in the Intra-rift Ridge and Low Velocity in the Deep, *EOS*, V 74, p. 666, 1993.
- Wiggins, Sean M., Canuteson Eric L., Dorman, LeRoy M., Hildebrand, John A., Sauter, Allan W., and Schreiner, Anthony E., Crustal Structure at the Hess Deep: Seismic Studies Show High Velocity and Density in the Intra-rift Ridge, *EOS*, V 73, p. 356, 1992.

FIELDS OF STUDY

Major Field: Marine Geophysics

Studies in Seismic Refraction

Professors LeRoy M. Dorman and John A. Hildebrand

Studies in Tomographic Inversion

Assistant Research Oceanographer Bruce D. Cornuelle and
Professor Guy Masters

Studies in Geology

Professor Peter F. Lonsdale

ABSTRACT OF THE DISSERTATION

Hess Deep Rift Valley Structure from Seismic Tomography

by

Sean Martin Wiggins

Doctor of Philosophy in Oceanography

University of California, San Diego, 1995

Professor LeRoy M. Dorman, Co-Chairperson
Professor John A. Hildebrand, Co-Chairperson

The Hess Deep rift valley, at approximately $2^{\circ} 14' N$, $101^{\circ} 33' W$, displays exposures of young, lower crustal and upper mantle rocks formed at the nearby, fast-spreading East Pacific Rise. A seismic refraction experiment was conducted across the Hess Deep rift valley to provide p-wave travel times between sea floor explosives and Ocean Bottom Seismometers. These travel time data were processed with an iterative, damped least-squares, inverse method to produce a velocity model of the subsurface structure. The resulting velocity contrasts were interpreted as lithologies originating at different depths and/or alteration of the preexisting rock units. Petrologic and bathymetric data from previous studies were used, along with the seismic interpretation, to produce a geologic model. The model supports low-angle detachment faulting with

serpentinization of peridotite as the preferred mechanism for creating the distribution and exposure of lower crustal and upper mantle rocks within the Hess Deep.

In addition to the geologic information gained from this study, linearity limitations of the tomographic inversion have been shown to be dependent on topography. Topography on the scale of the ray paths has been shown to effectively increase or decrease the velocity gradient, as does the Earth-flattening approximation. Valleys decrease the apparent velocity gradient; whereas, the converse is true for hills. If the velocity gradient is already weak (ie. at depths > 500 m in oceanic crust), then further decrease in gradient beneath a valley produces an environment where ray paths are highly sensitive to model change. Consequently, to avoid violating the linearity assumption, model changes beneath a valley must be smaller than for a hill or flat topography.

CHAPTER 1

Geologic Background

1.1 Introduction

A triple junction is a place where the boundaries of three lithospheric plates meet. The geometries, evolution, and stability of triple junctions were first discussed by *McKenzie and Morgan*, [1969]. They presented sixteen possible triple junction geometries between three possible plate boundaries: ridges (R), transform faults (F), and trenches (T). Only the RRR-type was found to be unconditionally stable; where stability was defined as conservation of junction geometry through the evolution of plate movement.

From magnetic anomaly data, *Raff*, [1968] postulated that a RRR-type junction exists west of the Galapagos Islands in the equatorial east Pacific where the Pacific, Cocos, and Nazca plates meet. On a regional scale, at approximately 2° N, 102° W, the East Pacific Rise (EPR) is intersected by the Cocos-Nazca Rise, to form the triple junction (Figure 1.1, modified from *Hey et al.*, [1986]). Bathymetric and magnetic data from *Hey et al.*, [1972] provided further evidence of the existence of an RRR triple junction there.

High resolution bathymetric studies with multi-beam sonar have shown, however, that the Cocos-Nazca spreading center does not meet the EPR. In fact, the propagating tip of the Cocos-Nazca ends at least 60 km east of the EPR in the rift valley of the Hess Deep [*Lonsdale*, 1977 & 1985]. *Searle and Francheteau*, [1986] also support this result with GLORIA sidescan sonar data. Further investigation of the area led *Lonsdale* [1988], to the discovery of the Galapagos microplate. The 13,000 km² microplate is bounded by the fast spreading EPR to the west, an incipient spreading

center to the north, the Dietz Basin to the south, and the Hess Basin at the tip of the Cocos-Nazca spreading center to the east (Figure 1.2, from *Lonsdale*, [1988]). Two RRR-type triple junctions occur in the region, one at the northern boundary of the microplate where the Pacific, Galapagos, and Cocos plates meet at $2^{\circ} 40' N$ [*Lonsdale*, 1988 & *Lonsdale et al.*, 1992], and the other at the southern end where the Pacific, Galapagos, and Nazca plates meet at $1^{\circ} 10' N$ [*Searle and Francheteau*, 1986]. It is the feature to the east of the Galapagos microplate, the Hess Deep rift zone, that is the focus of this study.

1.2 Regional Setting: Hess Deep

The Hess Deep, at $2^{\circ} 14' N$, $101^{\circ} 33' W$ and over 5000 meters below sea level (mbsl), was first discovered and named by *Hey et al.*, [1972]. The north-east pull of the Cocos plate coupled with the south-east pull of the Nazca plate have opened a valley at the tip of the westward propagating Cocos-Nazca spreading center. The rift valley is considered to be composed mainly of young (~ 1 Ma) EPR crust [*Lonsdale*, 1988]. For this area to remain geometrically stable, the Cocos-Nazca spreading center must propagate westward at the same rate that the EPR spreads new oceanic crust eastward, at the fast half-spreading rate of the 6.5 cm/yr. In contrast, the Cocos-Nazca spreads in the north-south direction at much slower half-spreading rate of 2.1 cm/yr [*Searle and Hey*, 1983].

The unusual topographic structure of the region raises questions on how the rift valley was formed. Figure 1.3a is a bathymetric map generated from *Sonne*, *Atlantis II*, and *Thomas Washington* SEABeam data. The marginal rift walls of the Hess Deep graben, composed of EPR crust, have been uplifted. Seven km south of the Deep, rising 2-3 km at a slope of 45° , is a horst that is tilted slightly southward; whereas, the northern shoulder, approximately 14 km from the Deep, has a greater tilt

($\sim 10^\circ$) and faces the north [*Lonsdale, 1988*]. Between the Deep and the northern rim is a flat crested intra-rift ridge rising to 3000 mbsl. The asymmetry normally associated with the low-angle detachment models for continental rift valleys formed by tectonic extension [*Wernicke, 1985*] is also observed at the Hess Deep region. Figure 1.3b shows the asymmetry of the north-south topographic cross-section (line AA') of the rift valley.

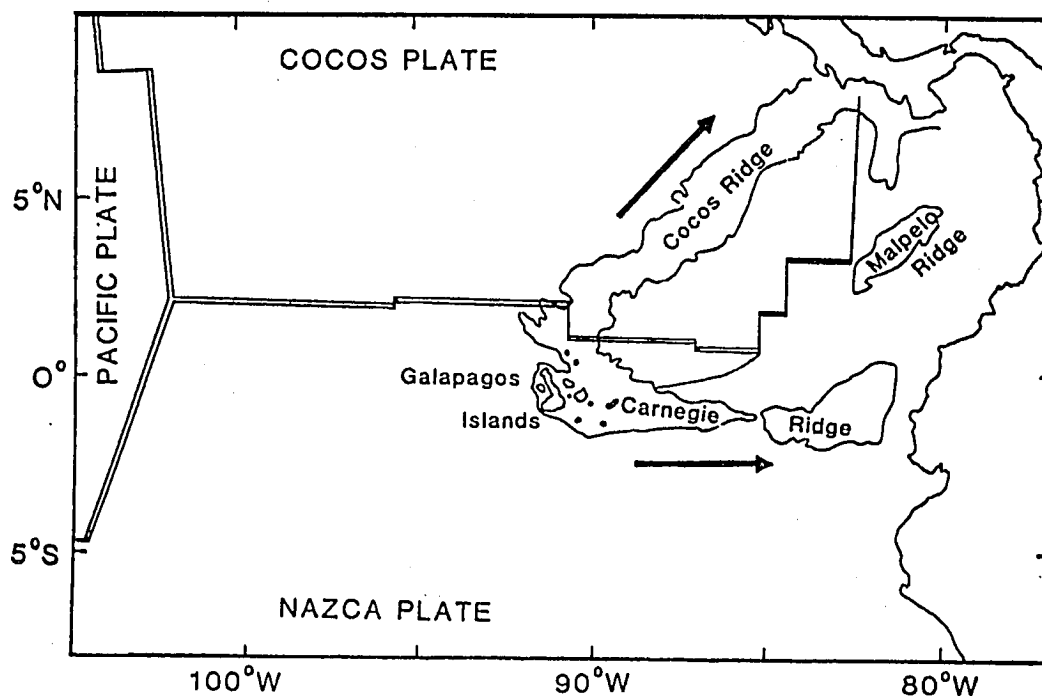


Figure 1.1. The originally conceived ridge-ridge-ridge triple junction at the intersection of the Cocos, Nazca, and Pacific plates. Modified from *Hey et al.*, [1986].

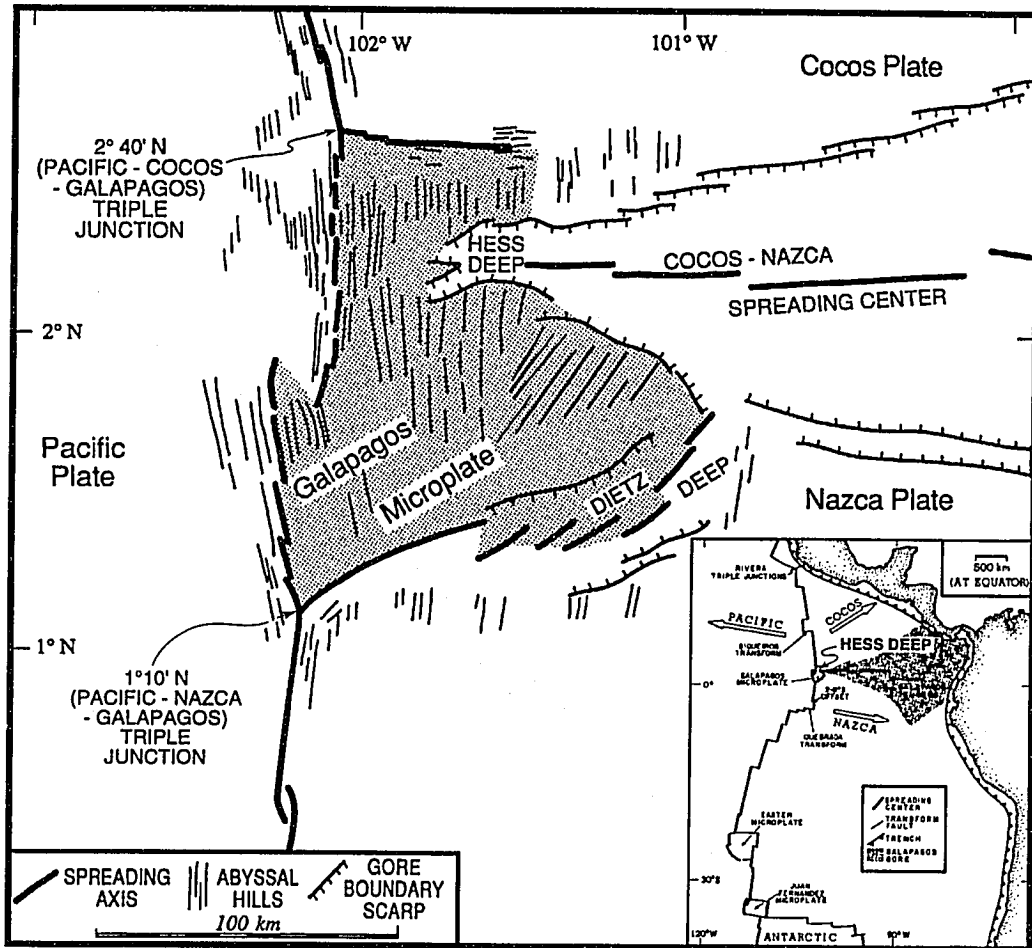


Figure 1.2. The Galapagos micro plate and its surrounding, which include the Hess Deep. From *Lonsdale*, [1988]. Inset: general area map from *Lonsdale*, [1992].

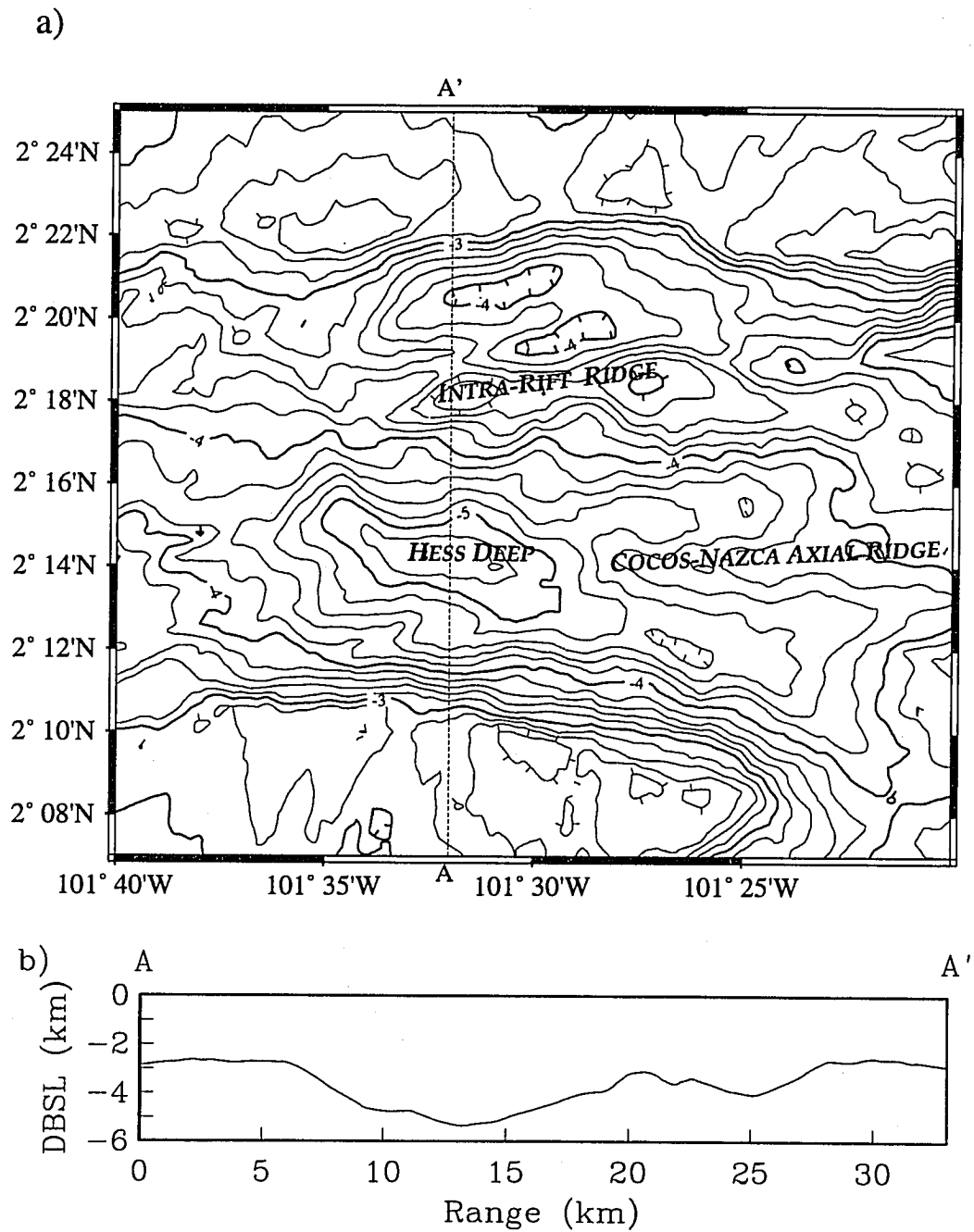


Figure 1.3. SEABeam data taken aboard the *Sonne*, *Atlantis II*, and the *Thomas Washington* used to generate a) Bathymetric plot of the Hess Deep rift valley and b) two dimensional cross section of rift valley at $101^{\circ} 32' W$ with no vertical exaggeration.

1.3 Petrology

The extension at the Hess Deep rift zone has produced an exposure of young oceanic crust formed at the nearby EPR. In addition to the crustal rocks dolerite and gabbro, upper mantle dunite and harzburgite (peridotites) are also exposed. The exposure of these deep, young, fast-spread rocks is unusual because tectonic extension with little or no magmatic intrusion is normally associated with slow-spreading ridges. Thus, the exposure provides a rare look into the sequence and formation of fast-spread oceanic crust and the upper mantle. Dredging and submersible surveys have been used to gather and view the surficial rocks at the Hess Deep. Gabbros and serpentized peridotites have been dredged from the foot of south side of the intra-rift ridge [Rudnik, 1976; Kashintsev *et al.*, 1982]. From the French submersible *Nautille*, Francheteau *et al.*, [1990] found the south flank of the Deep to consist of basaltic flows and dolerite dykes; whereas the 5400-plus m floor of Hess Deep was covered with sediment, gabbroic boulders, dolerite rocks and some young lava flows. On the north flank of Hess Deep, south of the intra-rift ridge, mostly gabbros and altered peridotites were observed. On the steep flanks of the intra-rift ridge an abundance of gabbroic rocks were surveyed. From the discontinuous outcrops of exposed rock in the Hess Deep area, Francheteau *et al.*, [1990] reconstructed the crust originating at the EPR and compared it to the ophiolite complex in Oman. The reconstruction aids in the understanding of the formation of oceanic lithosphere from a fast-spreading ridge. Figures 1.4 and 1.5 (from Francheteau *et al.*, [1990]) show the results of the *DSRV Nautille* dives and the *R/V Sonne* dredging.

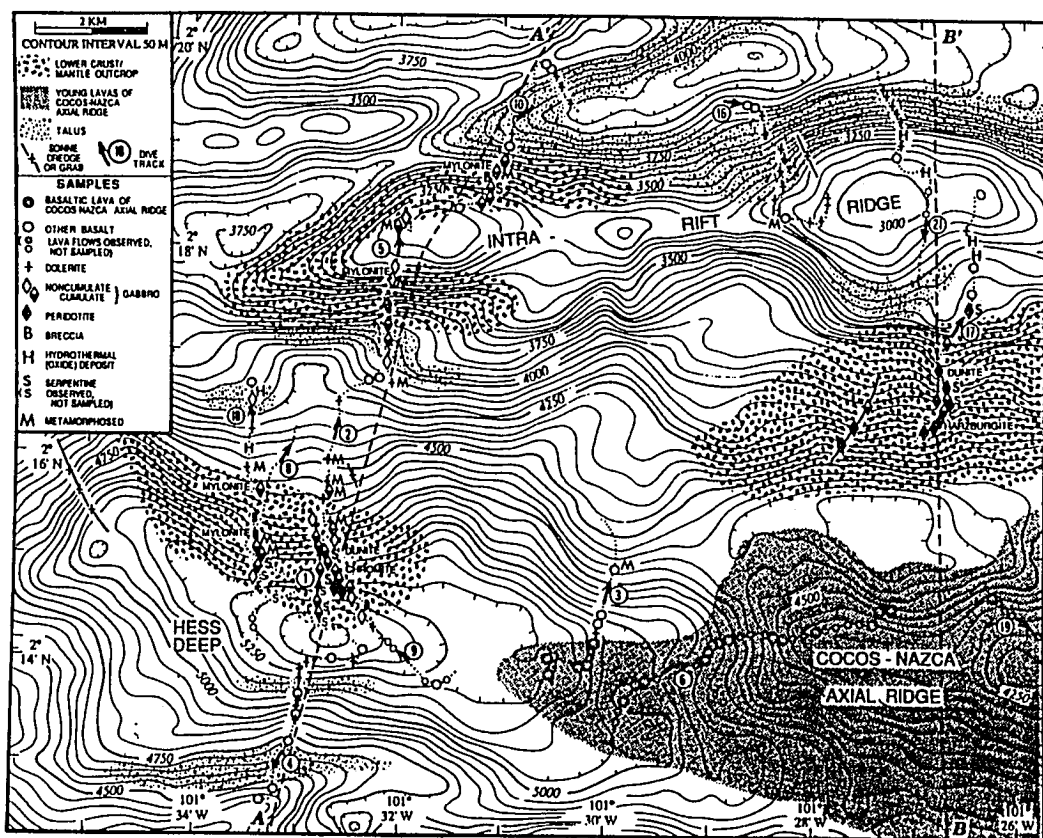


Figure 1.4. Petrological results of the *DSRV Nautila* dives and the *R/V Sonne* dredging of the Hess Deep region (from Francheteau et al., [1990]).

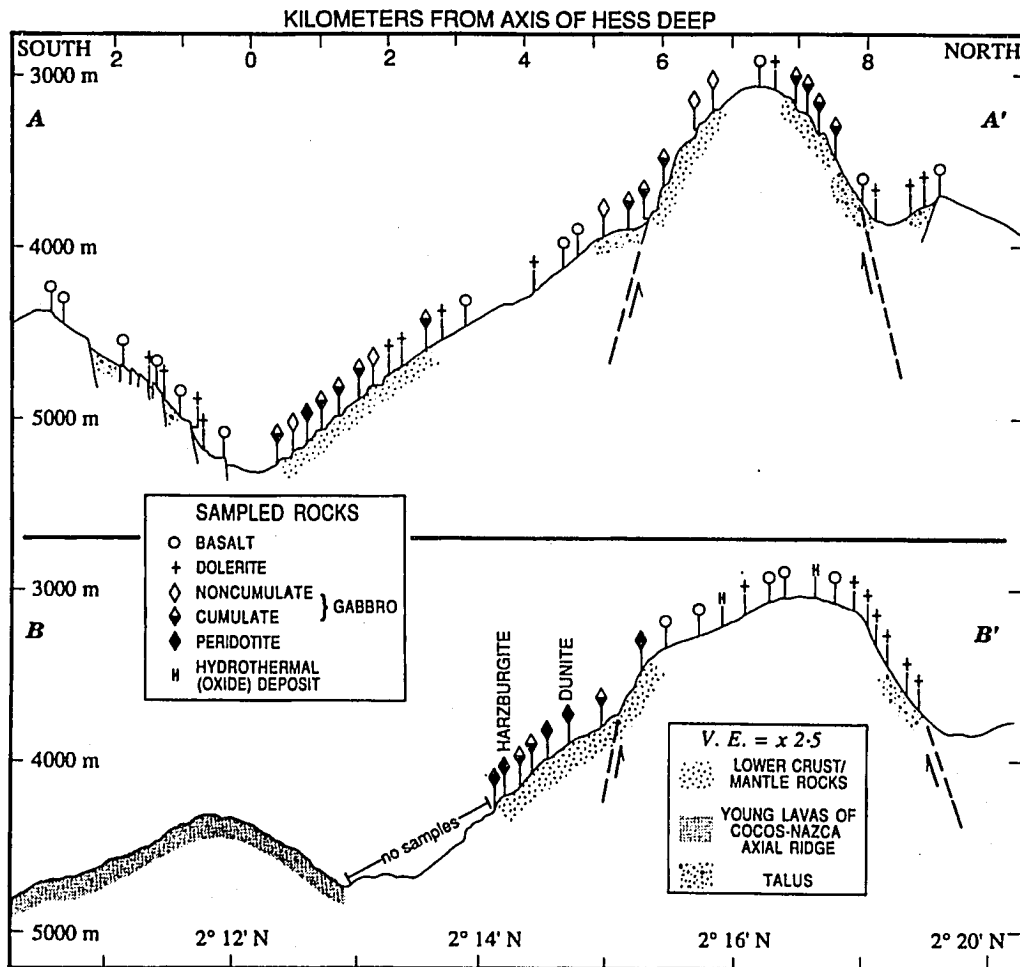


Figure 1.5. Petrological results of the *DSRV Nautila* dives and the *R/V Sonne* dredging of the Hess Deep region (from Francheteau et al., [1990]). Cross-sectional view.

1.4 Ocean Drilling Program

Leg 147 of the Ocean Drilling Program (ODP) was the first leg of a proposed hard-rock drilling project to reconstruct a composite section of fast-spread crust by drilling a number of offset holes in the Hess Deep rift valley. The primary goal of Leg 147 was to bring back a core that crossed the Moho discontinuity from lower crustal gabbros to the shallow mantle [JOIDES, 1992]. A long continuous section of this type, along with cores from other parts of the sequence, would yield valuable information on how plutonic crust is built. Even though the drilling conditions at the Hess Deep were unfavorable, plutonic rocks were cored on the crest of the intra-rift ridge at Site 894 [Gillis *et al.*, 1993]. The rocks were of gabbroic lithologies, the same as the *Nautila* program had recovered earlier. Site 895, east of the Deep, was the other drill location of Leg 147. Cores of shallow mantle peridotites were recovered, also agreeing with the findings of Francheteau *et al.*, [1990]. Unfortunately, the deepest hole drilled at the Hess Deep reached only 154 meters below the sea floor (mbsf). Magnetic inclination data taken from the cores at the two sites supports block rotation of $\sim 35^\circ$ around a horizontal axis [MacLeod *et al.*, in press]. This is consistent with the tectonic extension model of the Hess Deep [Francheteau *et al.*, 1990].

1.5 Geophysics

The geologic and bathymetric studies of the Hess Deep Basin have given a view of the surficial features of the rift valley and have provided much information on fast-spread oceanic crust. In order to gain further understanding of the tectonic processes that have taken place there, a "look" beneath the surface is needed. In April and May of 1992, we conducted geophysical experiments at the Hess Deep area in order to add to and form a more complete set of data upon which to base a geologic model. Shipboard and bottom gravity measurements were made along two north-south lines

transecting the rift zone. These data yield information about the average density of the rocks and lateral change in the densities. Along the same two lines, Ocean Bottom Seismometers (OBSs) were positioned. The OBSs recorded airgun, explosive sea floor shot, and earthquake data during the experiment. The airgun to OBS refraction data obtained provide a coarse average three-dimensional velocity structure of the Hess Deep. The many earthquakes recorded yield some information on the fault locations and focal mechanisms. The seafloor shot to OBS refraction data have given us a fine-scale two-dimensional velocity model of the area. It is the bottom shot refraction data that is the focus of this dissertation.

CHAPTER 2

Seismic Refraction Tomography Experiment at the Hess Deep

2.1 Introduction

In the spring of 1992, we performed a seismic refraction tomography experiment in the equatorial east Pacific at the Hess Deep rift valley. Tomography is the process of mapping an interior section of an opaque body. In this case, the earth is the opaque body and seismic velocity is the quantity being mapped. To image the subsurface velocity, we measure the time it takes for a compressional wave generated by a source to travel through the earth and be recorded by a receiver. These travel time measurements are the data that are then inverted to produce a model of velocity structure through the sampled area. The receivers used for the Hess Deep experiment were the autonomous Office of Naval Research (ONR) Ocean Bottom Seismometers (OBSs) [Sauter *et al.*, 1990] and the sources used were explosive sea floor shots [Dorman, 1993 & Hammer *et al.*, 1994].

2.2 Receivers

The OBSs employed at the Hess Deep sampled substructure velocity data from a 3-component seismometer at a rate of 128 Hz. Approximately 400 Mbytes, or 106 hours, of data were recorded per instrument on an optical disk. Anti-aliasing was performed with a four-pole filter, limiting the useful seismic signals to frequencies below 30 Hz. Two transceivers, 9 and 11 KHz, were also used on each OBS for acoustic navigation, instrument operation status, and ballast release for instrument recovery. An OBS was deployed by maneuvering the ship to a predetermined drop site and letting the instrument free-fall to the sea floor.

2.3 Sources

For sources, we used explosives detonated on the sea floor. In most active seismic experiments conducted at sea, the sources: airguns, waterguns, or explosives, are detonated near the sea surface. These shallow sources produce large footprints of acoustic energy on the sea floor, which is then converted into seismic energy. At a depth of 5000 meters, the first Fresnel zone (the region on the sea floor excited by the first half wave length of the acoustic energy) has a radius of approximately 700 meters for a source of 15 Hz. Given the rough topography at the Hess Deep, large errors in location of the energy entry point on the sea floor would result from near-sea surface sources. With sea floor shots, the seismic energy is directly coupled to the sea floor in a relatively small area. Another advantage to explosive sea floor shots is the direct production of shear and interface waves without the conversion from compressional water waves.

Each sea floor shot consisted of a plastic crate filled with approximately 30 kg of High Density Pentolite (comparable in energy and better under pressure than TNT) and a high pressure blasting cap wrapped in a "detaprime" (PETN) booster. After assembly, the explosive shots were lowered to the sea floor beneath a wireline electronics package called the rockscan sonar [Hammer *et al.*, 1994]. The rockscan sonar or shooter, suspended beneath the ship by 0.680" electromechanical wire, consisted of a transceiver, down looking sonar, eight charge firing ports, and the associated control telemetry. Up to six explosive packages were suspended from 0.32" wire, 15 meters apart with the shallowest one being 150 meters beneath the shooter. Once the ship was on site, the whole package was lowered so that the deepest shot was on the sea floor. After detonation the package was raised, the ship moved to the new source site and the process was repeated.

2.4 Experimental Layout

Two north-south lines of OBSs and explosive bottom shots were laid out at the Hess Deep (Figure 2.1). The geometry of the seismic experiment was chosen to provide ray sampling across the rift valley. The seismic lines followed the same general transects of the preceding submarine [*Francheteau et al.*, 1990] and dredging [*Rudnik*, 1976; *Kashintsev et al.*, 1982] surveys so that a comparison between surficial petrology and subsurface velocity structure could be made. In addition, the 12 km long east and 15 km long west lines were positioned to lay on top of the four proposed ODP drilling sites [*Dick et al.*, 1990] of which two were actually drilled (figure 2.1, sites 894 and 895). The seismic array geometry yields a two-dimension cross-sectional "view" into the substructure.

Spatial resolution of the resultant velocity model is dependent on the locations of the sources and receivers. The instrument spacing was approximately 2 km; whereas, the shots were positioned on the order of 1 km separation. The horizontal spacing provides approximately 1 km lateral resolution for the velocity model. Due to ray geometry, the vertical resolution is better than 1 km; however, the tradeoff is that only 2-3 km beneath the sea floor was sampled. Because the focus of the ODP group was on the west line site (figure 2.1), a larger data set was collected there and will be the emphasis of this study. Thus, only preliminary analysis of the east line data has been conducted.

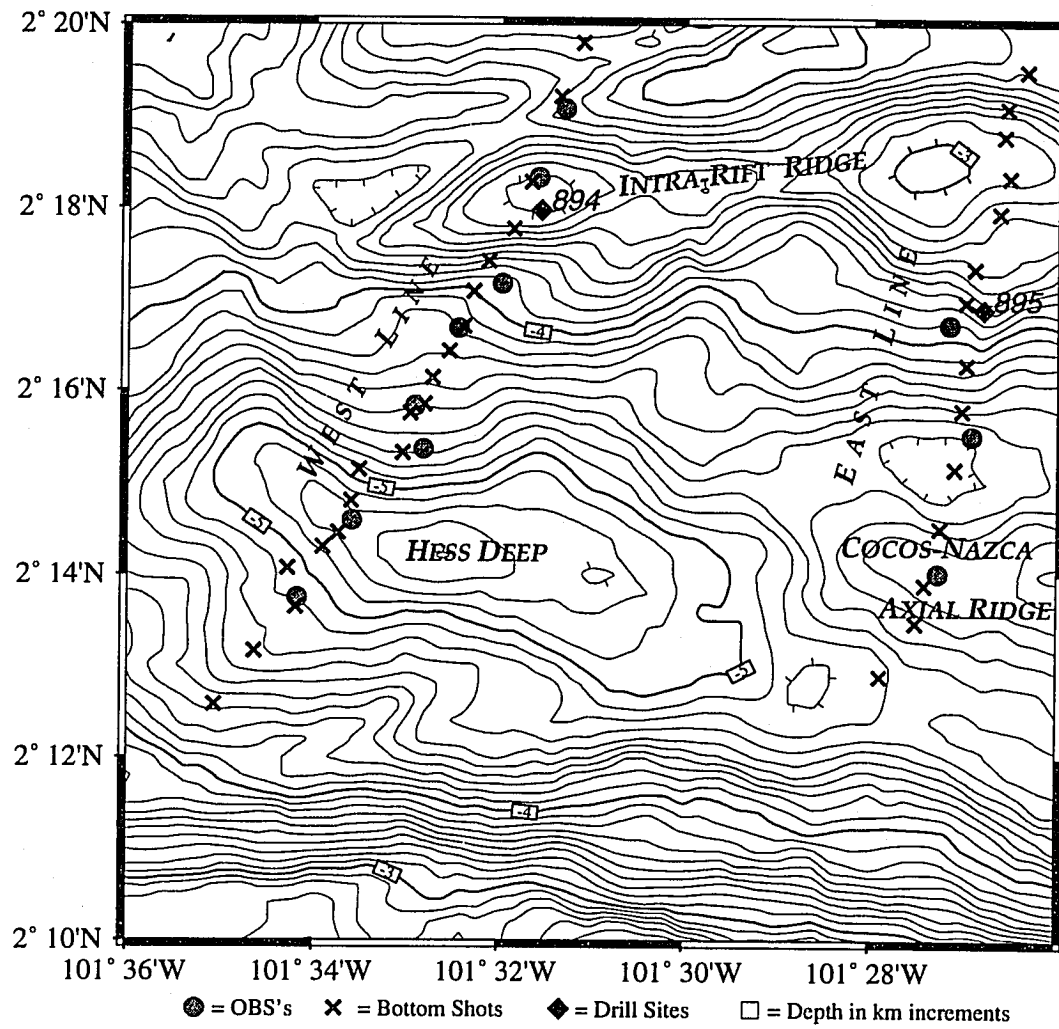


Figure 2.1. Refraction experiment source and receiver positions and bathymetry of the Hess Deep rift valley.

2.5 Source/Receiver Navigation

In refraction tomography, accurate receiver and source locations are essential. The accuracy of the resultant velocity model is partially dependent on the uncertainty of OBS and shot positions. After the OBSs were deployed, the ship received Global Positioning System (GPS) fixes while ranging to the instruments using 9 and 11 KHz transmit pings. If a given OBS received the transmit pulse it would issue a reply ping between 7 and 14.5 KHz. The ship to OBS acoustic travel time data were used with the ship's GPS data and a CTD sound speed profile of the water column to produce the navigated positions of the OBSs. The program implemented to accurately navigate the instruments uses generalized inverse theory (parameter estimation) [Creager and Dorman, 1982]. The forward problem is the calculation of the observables (instrument depth, travel times, and ship or fix location) from the parameters (latitude, longitude, and depth of OBS and latitude and longitude of the fix) by tracing the acoustic ray paths through the water column. The calculated and measured data were differenced and inverted to solve for the parameters (unknowns). The forward and inverse problems were iterated upon until the calculated and the expected uncertainties agreed ($\chi^2 \approx 1$). Using this method, relative instrument positions were found to be accurate within 10 meters (< 7 ms). Inverse methods will be discussed later.

Navigation of the bottom shots did not produce as accurate results as the navigation of the OBSs. Initially, the procedure was to navigate the shooter within an array of sea floor transponders. The array would provide good horizontal geometry for location of the shooter; whereas, depth would be constrained by the shooter's on board pressure gauge. By knowing the location of the shooter, the positions of the explosives could be deduced as directly beneath the apparatus. Using the inverse method briefly described above, the shooter could be accurately navigated relative to the transponder network. However, these positions would then need to be translated into the OBS

network. The incompatibility between the shooter/sea floor transponders and the ship/OBS transceivers acoustic systems made the translation between the two acoustic networks unreliable. The two networks could have been 'tied' together if the ship had ranged to the sea floor transponders and the OBS transceivers at relatively the same time. Because this was not the case, water wave arrivals from the explosive bottom shots to the OBSs were used. The *Creager and Dorman*, [1982] program was modified to accept sea floor-to-surface-to-sea floor and deep water direct ray paths in addition to the original surface-to-sea floor paths. In this case, the previously navigated OBS positions were used as the fixes and the shot positions were the unknown instrument locations. The rough topography at the Hess Deep made some direct path water waves impossible, but most of the surface bounce arrivals could be detected. Also, the geometry of the fix/instrument locations for the shot navigation was not as good as for the OBS navigation. The topography and geometry shortcomings coupled with shooter timing inaccuracies resulted in a shot navigational accuracy of 25 meters on the average and over 60 meters in the worst case. Although these uncertainties are larger than the ones found for the OBSs, they are still within the acceptable range.

2.6 Data

The time it takes for a compressional (P) wave generated by an explosive sea floor shot to travel through the substructure and reach an OBS is a datum. Data uncertainties result from P-wave picking errors, OBS clock initialization errors, OBS clock drift, and shot clock errors. Pick errors are on the order of 3 samples, or ~ 24 ms. The OBS clocks are high precision quartz Seascan clocks with drift less than 1 ms/day. The initialization of the OBS clocks and the firing of the shots were triggered with a Kinometrics GPS receiver resulting in timing errors less than 1 ms. Delays in shot detonation are presumed to be shooter hardware related and are solved for in the shot

navigation inversion previously discussed. The largest source of data uncertainty from the 130 recorded shot to OBS pairs is the pick uncertainty. A representative record section plot from OBS 4 on the west line is shown in Figure 2.2. This instrument is approximately half-way up the south flank of the intra-rift ridge, north of the Deep (approximately $2^{\circ} 16' N$). On the plot, the OBS is at 0 km range, the shots to the north are positive range and the shots to the south are negative. The data are picked from the first arrival, the P-wave. Note the high frequency, large amplitude arrivals later in the record section; these are the direct water wave arrivals. In the negative range, to the south, they are easily seen; whereas, to the north only one or two water wave arrivals can be picked. The absence of the direct water waves is caused by the acoustic shadowing effect from the rough topography at the Hess Deep. Figure 2.3 is a record section of the same data with the time axis reduced by the range from the OBS to the shot per 4.5 km/sec. The plot yields the first qualitative view of the substructure. If the rock were homogeneous with an average velocity of 4.5 km/s, then the first arrival of the P-waves would line up horizontally. Note, however, the asymmetry between the northern and southern P-wave arrivals. Because P-wave travel time is proportional to velocity, asymmetry in the velocity structure can be deduced. For example, at approximately 3 km range the P-wave from the northern shot arrives before the one to the south, exhibiting higher velocity structure to the north. This gives some clues as what to expect from a more quantitative analysis of the data through tomographic inversion.

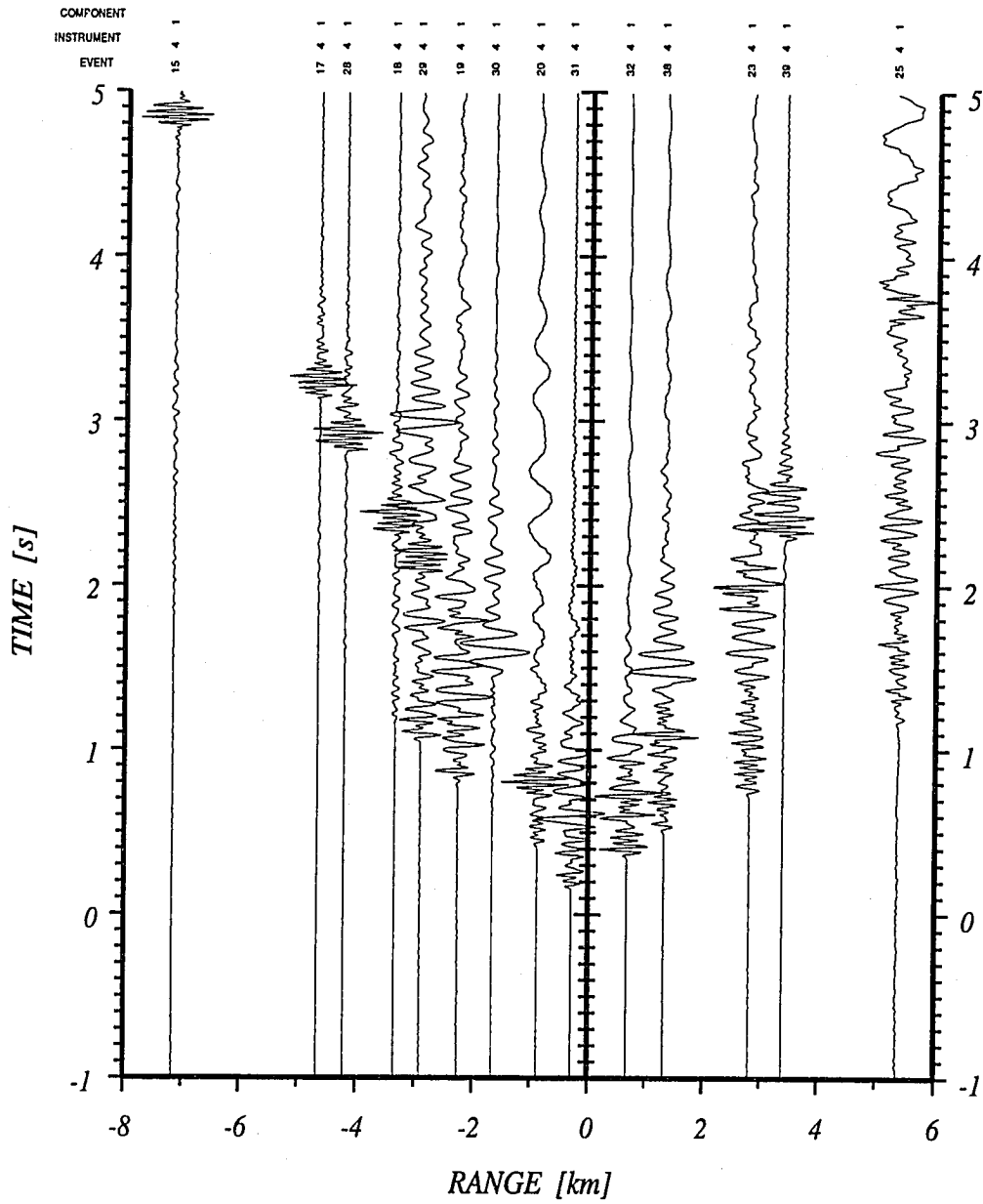


Figure 2.2. Record section for OBS 4 on the west line. The instrument is approximately half-way up the south facing flank of the intra-rift ridge.

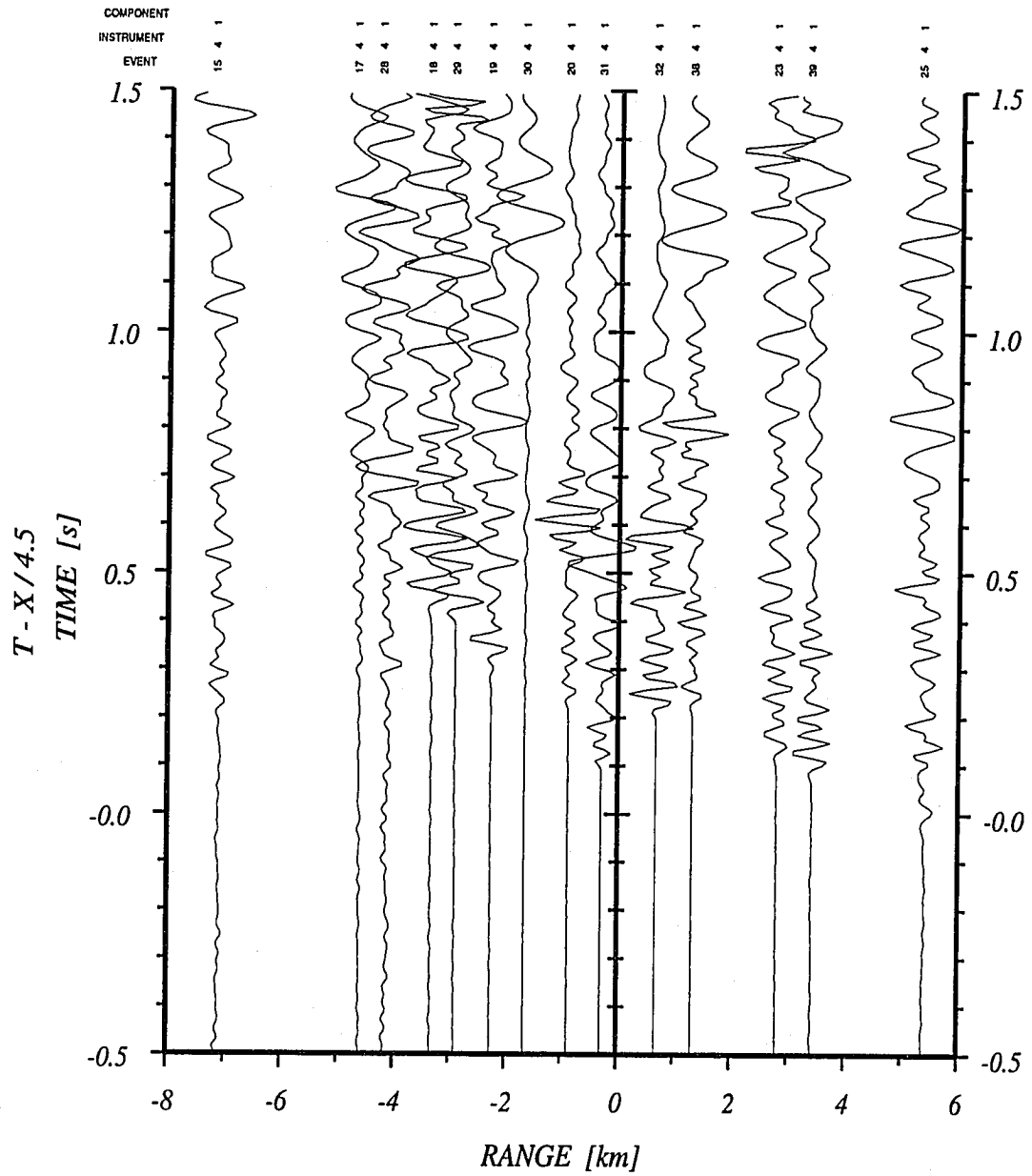


Figure 2.3. Reduced time (4.5 km/s) record section for OBS 4 on the west line.

CHAPTER 3

Data Processing Techniques

3.1 Introduction

The main objective in a seismic refraction study is to produce a velocity model that is representative of the sampled structure. The P-wave travel time data are used in an inverse approach to create a model. The procedure used for the Hess Deep seismic tomographic inversion can best be illustrated in a flow chart (figure 3.1). First, an estimate is made of the average velocity structure of the studied region. Seismic rays are then traced from source to receiver in the starting model, yielding calculated travel times. The model is parameterized (represented as a finite set of predetermined basis functions) for purposes of the inverse. The relationship between the travel time data and the velocity model is linearized around the initial guess by allowing only small changes in the model parameters, which in turn produce small, nearly linear changes in the data. The differences between the measured and calculated travel times are used as the data for the inverse to estimate the correction needed for the assumed model. The data uncertainties are set according to the expected size of the nonlinearities resulting from tracing incorrect ray paths and travel time picking errors. The forward problem matrix, \mathbf{G} , is calculated using the ray path and parameterization information. Next, a damped least-squares inverse is performed on the data. The result is a correction to the starting velocity model. The linearity assumption is monitored to make sure it is not violated within the assumed error bars. A new model is generated by adding the correction to the starting model. A penalty measure based on *a priori* error estimate is checked if it has been minimized indicating that the final model has been reached. If not, the process is repeated beginning with tracing rays through the new model. The

following is a description of the iterative data processing techniques and synthetic examples showing the strengths and weaknesses of this method.

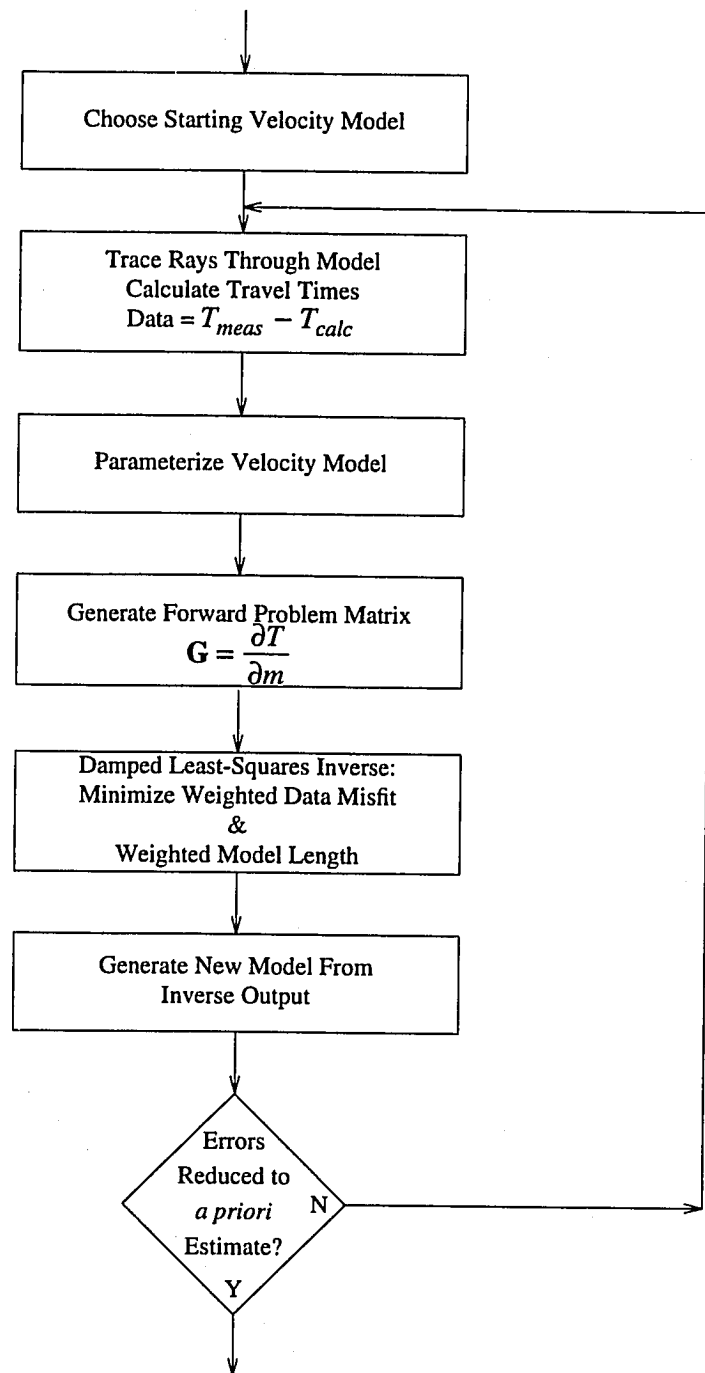


Figure 3.1. Flow chart of data processing method

3.2 Starting Model

The first step in finding a velocity model representative of the sampled region is choosing a starting, or reference, model. In seismic refraction, the relationship between the travel time data with fixed source/receiver spacing and the model velocity distribution is nonlinear; therefore, we would like to start with a model that is reasonably close to the final model so that a small number of iterations are required to reach a solution. We generate an average one-dimensional (depth dependent) velocity profile of the Hess Deep by solving a one step inverse using a one-dimensional layered starting model similar to the findings of *Vera et al.* [1990] for fast-spread EPR crust (figure 3.2). This starting model was chosen for the one-dimensional inverse because the crust in the Hess Deep region originated at the nearby EPR [*Lonsdale, 1988*]. Once the coarse vertical features of the study area have been resolved, the average Hess Deep velocity profile is then used as the reference model in an iterative inverse to solve for lateral variations in the velocity structure. The one-dimensional velocity profile, consisting of constant velocity gradient layers, is 'hung' from the bathymetry producing a three-dimensional velocity model. We call this type of model 'laterally' homogeneous because at a given depth beneath the sea floor the velocity is the same, independent of range. In physical space (x,y,z) , the geometry of the velocity model is chosen such that the x -direction is along the OBS/shot line (rotated $\sim 30^\circ$ clockwise from North), the y -direction is across the OBS/shot line, and the z -direction is beneath the sea floor. The model's dimensions are 17 km by 1.6 km by 5 km and is gridded 100 m by 400 m by 100 m in x , y , and z , respectively.

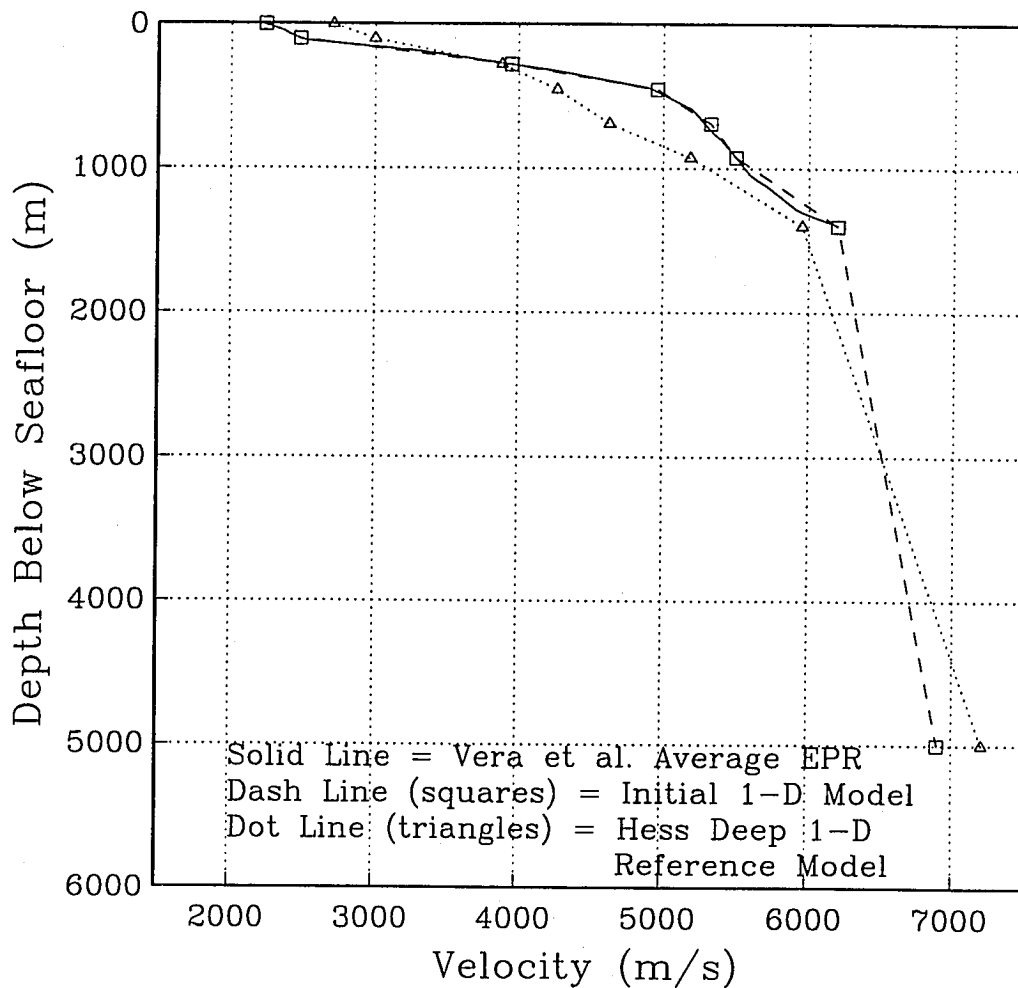


Figure 3.2. One-dimensional velocity profiles 'hung' from bathymetry to produce three-dimensional velocity models. Solid line is average East Pacific Rise crust from *Vera et al.*, [1990]. Dashed line is the one-dimensional layered starting model for a one step inverse. Dotted line is the result of the one step inverse which serves as the Hess Deep reference model. The squares represent the velocity values of the vertical model parameters, $m_{i,j=0}$, at fixed depths.

3.3 Ray Tracing

Once a three-dimensional velocity model has been made, seismic rays are traced through it producing calculated travel time data. A simplistic, but fast, two-dimensional ray tracing algorithm is used in which ray paths arcs in regions of constant velocity gradients are added together to form the whole ray path. The results of this algorithm are tested against an analytical expression for ray travel time in a constant velocity gradient medium and agree within 1 msec given a source/receiver spacing of approximately 5 km. The ray traced calculated travel times are subtracted from the experimental observed travel times to produce the data used in the inverse.

3.4 Parameterization

Parameterization of the velocity structure is needed for this form of the inverse problem. Parameterization is the representation of the physical model as parameters, or coefficients, of mathematical basis functions. There are many ways to parameterize a heterogeneous structure, each with advantages and disadvantages. For example, modeling the structure as blocks, or layers, creates a parameterization that can resolve discontinuous features and is easy to visualize; however, the result can be dependent on the location and size of the blocks and cause ray tracing difficulties due to a sharp changes in velocity structure. On the other hand, functions that are differentiable everywhere can impose a smoothing constraint and provide models less likely to cause ray tracing problems. We chose to represent the velocity model vector as the coefficients, or parameters, of a linear combination of infinitely differentiable functions (i.e. sines and cosines) horizontally, and first-order differentiable layers (i.e. triangle functions) vertically.

The model is parameterized horizontally in the x -direction and vertically in the z -direction. There is no additional parameterization along the rift axis, in the y -direction, because the ray paths run mostly along the source/receiver line and the heterogeneity of the substructure is minimal across-line for the relatively short width of the model. The vertical parameterization is accomplished by using layers of constant velocity gradients because young oceanic crust is considered to be layered lithologically and with respect to velocity. Even if the region is lithologically scrambled, as presumed at the Hess Deep, overlying pressures will approximately maintain a layered relationship between velocity and depth. Denoted by a v superscript, the vertical parameterizing functions are

$$f_i^v(x,y,z) = \frac{z_{i+1} - z'(x,y,z)}{z_{i+1} - z_i}$$

and

$$f_{i+1}^v(x,y,z) = \frac{z'(x,y,z) - z_i}{z_{i+1} - z_i}$$

where, $z'(x,y,z) = z - b(x,y)$ is between layer interfaces i and $i+1$ beneath the sea floor, $b(x,y)$, and is positive downward in the z direction. Figure 3.3 is a plot of the vertical functions. At a given $z'(x,y,z)$ between layer interfaces, the two functions reproduce the constant velocity gradients of the one-dimensional velocity profile in figure 3.2 using function coefficients (model parameters, $m_{i,j=0}$) corresponding to the velocity at the nodal depth, z_i . For example, at $z'(x,y) = 450$ meters beneath the sea floor, $f_4^v(x,y,z) = 1$ and $m_{4,0} = 3950$ m/s (see figures 3.2 and 3.3).

The horizontal parameterization is accomplished by using Fourier harmonics making it easy to impose a smoothing constraint by adjusting the expected variances of each Fourier component (i.e., higher wavenumbers have smaller variances). The

horizontal smoothing constraint originates from the assumption that at a given depth and close spacing (i.e. < 1 km) the rock velocities will be similar on the average. Denoted by an h superscript, the horizontal functions are

$$\begin{aligned}
 f_j^h(x) &= 1 && \text{for } j = 0 \\
 &= \cos \left[\frac{j2\pi x}{L_x} \right] && \text{for } j \text{ even} \\
 &= \sin \left[\frac{j2\pi x}{L_x} \right] && \text{for } j \text{ odd}
 \end{aligned}$$

where, L_x is twice the length of the model, 34 km, in x . Combining the horizontal and vertical parameterization, the velocity model is defined:

$$v_o(x, y, z) = \sum_{i=0}^{N-1} f_i^v(x, y, z) \sum_{j=0}^{M-1} m_{i,j} f_j^h(x) \quad (3.1)$$

The starting model is constrained to be 'laterally' homogeneous with respect to the topography; thus, the horizontal parameters ($m_{i,j \neq 0}$) are initially set to zero and become non-trivial as the inverse estimates the lateral heterogeneity of the velocity structure. There are $M = 33$ horizontal parameters for each of the $N = 9$ vertical parameters for a total of 297 model parameters. The number of horizontal parameters are chosen to produce a minimum half-wave length that is approximately 1 km. The 1 km resolution limitation is imposed by the experimental geometry: source/receiver spacing, ray coverage, and ray wave length. The vertical parameters are not as equally distributed with more resolution in the upper layers because the ray density is higher near the sea floor.

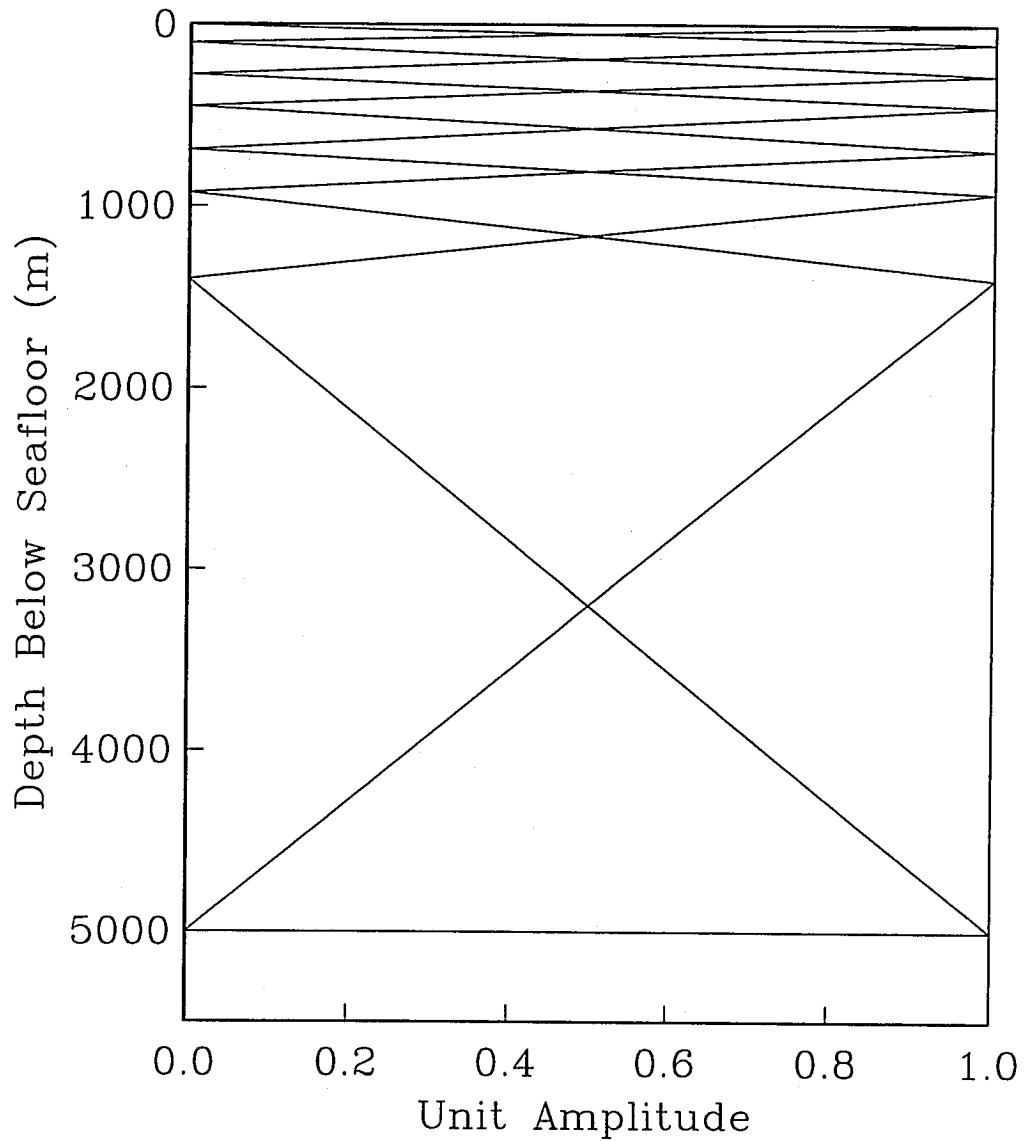


Figure 3.3. The vertical functions used in parameterization. Triangle functions, $f_i^v(x,y,z)$, are used to linearly interpolate the velocity value between two interfaces. These functions, along with their respective coefficients, reproduce the one-dimensional velocity profile shown in figure 3.2.

3.5 Forward Problem Matrix Calculation

The forward problem matrix, or Green's matrix, \mathbf{G} , linearly relates the travel time data to the velocity model:

$$\mathbf{d} = \mathbf{G}\mathbf{m} + \mathbf{n} \quad (3.2)$$

where, \mathbf{d} is the data vector, \mathbf{m} is the model vector, and \mathbf{n} is the noise vector. The time, T_k^o , it takes for ray k to travel along ray path Γ_k^o through the model v_o is the integral of the slowness along that path:

$$T_k^o = \int_{\Gamma_k^o} \frac{ds}{v_o(x,y,z)} \quad (3.3)$$

where, ds is the differential ray path. The true velocity structure can be written as the sum of the velocity model and a velocity perturbation:

$$v(x,y,z) = v_o(x,y,z) + \delta v(x,y,z) \quad (3.4)$$

where, $\frac{\delta v}{v_o} < 1$ by assumption. Substituting equation (3.4) into the true travel time equation (similar to equation (3.3)) yields

$$T_k = \int_{\Gamma_k} \frac{ds}{v_o(x,y,z) + \delta v(x,y,z)} + n_1 \quad (3.5)$$

where, n_1 is the experimental noise due travel time picking and instrument location and timing uncertainties. Doing a Taylor series expansion of the integrand while treating higher order terms as noise, n_2 , produces

$$T_k = \int_{\Gamma_k^o} \frac{ds}{v_o(x,y,z)} - \int_{\Gamma_k^o} \frac{\delta v(x,y,z)}{v_o^2(x,y,z)} ds + n_1 + n_2 + n_3 \quad (3.6)$$

where, n_3 is the noise due to assuming a ray path of Γ_k^o instead of the true ray path Γ_k . It should be noted that if the problem were cast in slowness instead of velocity then

$n_2 = 0$; however, the relative magnitude of this term compared to the other noise terms is very small and does not cause any noticeable nonlinearity effects.

Equations 3.3 and 3.5 are nonlinear. The relationship is linearized to allow the use of a linear inverse. Approximate linearity is achieved by forcing changes in the model to be small which produce proportionately small changes in the data. How small the model changes must be kept in order to preserve the linearity of the problem and the factors which limit these changes, or step sizes, is discussed in chapter 5. Under the linearity assumption, the travel time residuals (the observed minus ray traced calculated travel times, δT_k) are the data vector, \mathbf{d} , of equation (3.2) and the perturbations to the velocity model parameters, $\delta m_{i,j}$, are the model vector, \mathbf{m} . Thus, from equation (3.1), the velocity perturbation is

$$\delta v(x, y, z) = \sum_{i=0}^N f_i^v(x, y, z) \sum_{j=0}^M \delta m_{i,j} f_j^h(x) + n_4 \quad (3.7)$$

where, n_4 is the noise introduced from parameterization inadequacies creating an inability to model the real structure exactly. Substituting equation (3.7) into (3.6) and rearranging we have

$$\delta T_k = T_k - T_k^p = - \sum_{i=0}^N \sum_{j=0}^M \int_{\Gamma_k^p} \frac{ds}{v_o^2(x, y, z)} f_i^v(x, y, z) f_j^h(x) \delta m_{i,j} + n_1 + n_2 + n_3 + n_4$$

which is equivalent to equation (3.2). Thus, an element of the forward problem matrix, or Green's matrix, is

$$G_{i,j}^k = - \int_{\Gamma_k^p} \frac{ds}{v_o^2(x, y, z)} f_i^v(x, y, z) f_j^h(x). \quad (3.8)$$

3.6 Inverse Procedure

The forward problem uses equations (3.2) and (3.8) to map linearly a model vector, \mathbf{m} , into the data vector, \mathbf{d} . However, the ultimate goal in seismic refraction tomography is to use the data to obtain a model representative of the sampled earth. This is accomplished by doing the 'backwards' problem or inverting the data. A linear stochastic (damped least-squares) inversion [Franklin, 1970; Aki & Richards, 1980] is used to construct a model vector for the Hess Deep. The approach and code, developed by Cornuelle *et al.* [1989], has been successfully adapted from ocean acoustic tomography to seismic tomography by Hammer *et al.* [1994] for the Jasper Seamount seismic refraction study. We use the same methods iteratively for the Hess Deep.

We consider that both the model vector, \mathbf{m} , and the noise vector, \mathbf{n} , are random variables with zero means, $\langle \mathbf{m} \rangle = \langle \mathbf{n} \rangle = 0$ and that their covariances are given by $\langle \mathbf{m}\mathbf{m}^T \rangle = \mathbf{R}_{mm}$ and $\langle \mathbf{n}\mathbf{n}^T \rangle = \mathbf{R}_{nn}$, respectively. The diagonals of the covariance matrices are the expected uncertainty variances of the model parameters and the data noise. The model variance used is approximately 600 m/s in each layer. The model covariance was chosen to give a $(1/e)$ horizontal decorrelation scale of approximately 2 km. The noise variance used is 50 msec and was estimated during the iterative inverse using the tradeoff between fitting the data and minimizing the model. The best estimate, $\hat{\mathbf{m}}$, of the true model, \mathbf{m} , is determined by minimizing the data misfit and model length weighted by their respective covariances:

$$\text{minimum} = (\mathbf{d} - \mathbf{G}\hat{\mathbf{m}})^T \mathbf{R}_{nn}^{-1} (\mathbf{d} - \mathbf{G}\hat{\mathbf{m}}) + \hat{\mathbf{m}}^T \mathbf{R}_{mm}^{-1} \hat{\mathbf{m}} \quad (3.9)$$

Equation (3.9) shows that the solution to the stochastic inverse is a trade-off between the L_2 norm of the travel time residuals minus the calculated forward problem data and the L_2 norm of the perturbations of the model parameters. Minimizing equation (3.9), by differentiating with respect to $\hat{\mathbf{m}}$ and setting it equal to zero, and solving for $\hat{\mathbf{m}}$ we

have the solution:

$$\hat{\mathbf{m}} = \mathbf{R}_{mm} \mathbf{G}^T \left[\mathbf{R}_{nn} + \mathbf{G} \mathbf{R}_{mm} \mathbf{G}^T \right]^{-1} \mathbf{d}. \quad (3.10)$$

The terms to the left of the data vector are the linear operator for the damped least-squares inverse.

Under ideal conditions, a solution is chosen by the inverse from the Green's matrix, minimizing the weighted variances of the model plus data in a single step. However, the rough topography at the Hess Deep limits the linear model perturbation magnitude so that a final solution cannot be reached in one step. Chapter 5 discusses the limitations of the linearity assumption due to topography. Multiple iterations are used to arrive at a final model. The expected data uncertainties are adjusted so that the noise in equations (3.2) and (3.10) is consistent with the errors due to travel time picking and the nonlinearities from incorrect ray paths. The new model estimate is then used as the next reference model and the above process is repeated. The iterative final solution is obtained similarly to a one-step damped least-squares in that the trade-off between the weighted data residuals and weighted model length is considered. The data residuals are caused by the noise terms discussed the previous section. The model length is a measure of the structure added to the reference model. The weighted penalty norm of the model parameter estimate is increased by increasing model structure spatially and in magnitude. If the model structure is limited to large spatial features, then the inverse can only increase the magnitude of the features to further minimize the data residuals. However, large changes in the velocity structure at small distances can make ray tracing difficult due to the introduction of triplications and caustics. The final model is reached once the data residuals decrease to a level where a decrease in the weighted data penalty function requires an equal increase in the model parameter penalty function. In addition, the model structure is not permitted to

increase enough to cause a significant amount of data (ray) loss.

3.7 Synthetic Example

Synthetic examples are presented as illustrations of the performance of the iterative inverse process. The known synthetic velocity fields are treated as true earth models. Rays are traced through the synthetic bodies to produce travel times that are a substitute for the real, observed data. These data are used to show the resolving power of the damped least-squares inverse. Additional Gaussian random noise is added to the synthetic data to demonstrate the effect of noise on the solution. Three regions are investigated independently with the synthetic modeling: the valley of the Deep, the incline or slope from the Deep up to the intra-rift ridge, and the hill or dome of the intra-rift ridge. The same parameterization scheme, penalty function weighting, and source/receiver pairing and geometry used in the real inverse are used to try to resolve the test velocity fields. To avoid nonlinearity effects, small steps (model velocity changes < 100 m/s) are taken to arrive at a solution as in the analysis of the real data.

The synthetic velocity field used for the three regions is the three-dimensional reference velocity model generated from the Hess Deep one-dimensional velocity profile (figure 3.2 and 3.4a) along with a low velocity intrusion. A low velocity intrusion is a reasonable choice for a synthetic body because it is similar to serpentinite diapirs that are postulated to be present in the Hess Deep region [Francheteau *et al.*, 1990]. At a given depth beneath the topography of the model, the low velocity perturbation is homogeneous in the y -direction and ramps parabolically from zero to a -1000 m/s perturbation in the x -direction. The intruded structure spans z from 275 meters beneath the sea floor to the bottom of the model and is 3 km wide at the start of its ramp. Figure 3.5 is a plot of the synthetic structures for the three regions. The plots show the two-dimensional cross section of the west line with depth below the sea surface and

range along the OBS/shot line. Contours are every 200 m/s and the 0 m/s contours are annotated to help with visualization between positive and negative values in the following grayscale plots. The location and geometry of the ray paths (figure 3.4b) indicate where the model is well sampled and, consequently, where the inverse is expected to resolve the synthetic structure well. For example, the ray density and crossings are high a few hundred meters beneath the sea floor which indicate good resolving power; whereas, deeper in the model the sparse ray coverage weakens the resolution of the synthetic body. In addition to the imperfect ray coverage, the intruded low velocity structure was generated independently of the finite Fourier series used to parameterize the model in the horizontal; therefore, we expect a solution that is smeared/smoothed with the sharp lateral discontinuities unresolvable.

Figure 3.6 shows the results of the iterative damped least-squares inverse for the three regions investigated. Because there is no sampling of the model beneath the deepest ray paths, the lower part of the plots have been omitted. Minimization of equation 3.9, using the same weights used in the real inverse, is carried out with the synthetically generated data and no additional noise. In all three cases, the low velocity intrusion is resolved reasonably well. As expected, the results are smeared and show peak values where the ray coverage is best. This noise-free simulation isolates the errors due to imperfect ray sampling. To illustrate the sensitivity of the iterative inverse to data errors, random noise is added to the three sets of noise-free data.

In the case of the real inverse, the RMS of the data residuals is 50 msec. Figure 3.7 shows three independent sets of normally distributed noise with zero mean and 50 msec standard deviation as a function of the range of the ray turning point. The noise is added to the three sets of noise-free synthetic data to produce new sets of data to invert. These new data sets have lower signal-to-noise ratios than the real data, but still provide a reasonable way to illustrate the effects of random noise on the resolving

power of the inverse method. Figure 3.8 shows the results of the iterative inverses using the noisy data. The low velocity intrusion is partially resolved in all three case; however, not as well as with the noise-free data. In addition, the noise adds some structure beyond the smoothed limits of the intrusion, but small scale model perturbations with peak values of a few hundred m/s are still within the predefined model RMS error bounds. The same penalty weighting of the model length and data residuals used in the real inverse for the minimization of equation 3.9 was used for both sets of simulations. The 50 ms weighting of the data fit penalty function prevents the inverse from being too sensitive to data noise or producing a model that over-fits the data.

Figure 3.4 Reference model and ray paths a) Reference velocity model constructed by "hanging" Hess Deep 1-D model (figure 3.2) from bathymetry. b) Ray paths traced through reference model. Dense ray coverage and multiple near-perpendicular crossings indicate regions that can be well resolved.

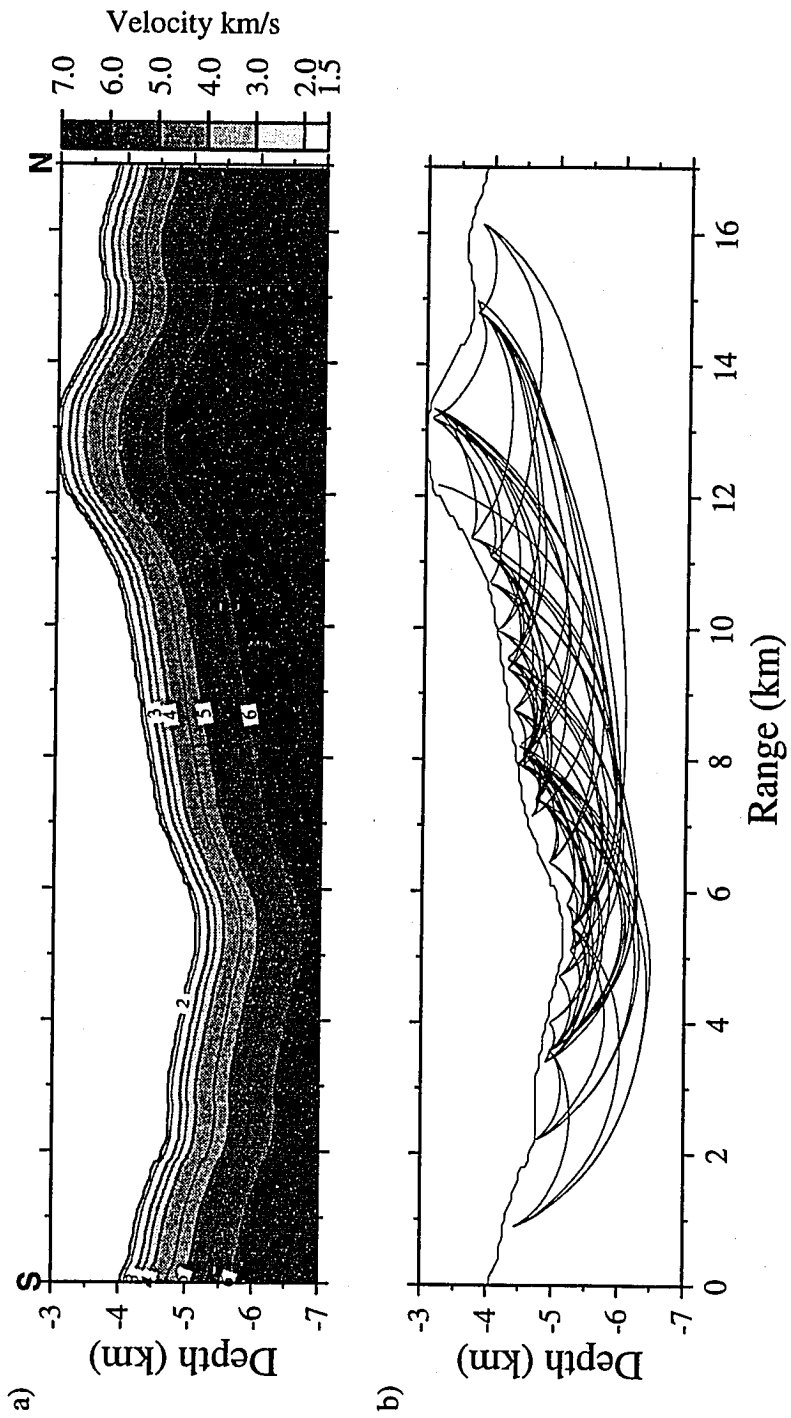


Figure 3.5 Intruded low velocity perturbation. The amplitude of the perturbation rises parabolically along range from zero to 1000 m/s. The width of the intrusion is 3 km. a) The low velocity perturbation is intruded beneath the valley, b) beneath the incline from the valley to the ridge and, c) beneath the intra-rift ridge.

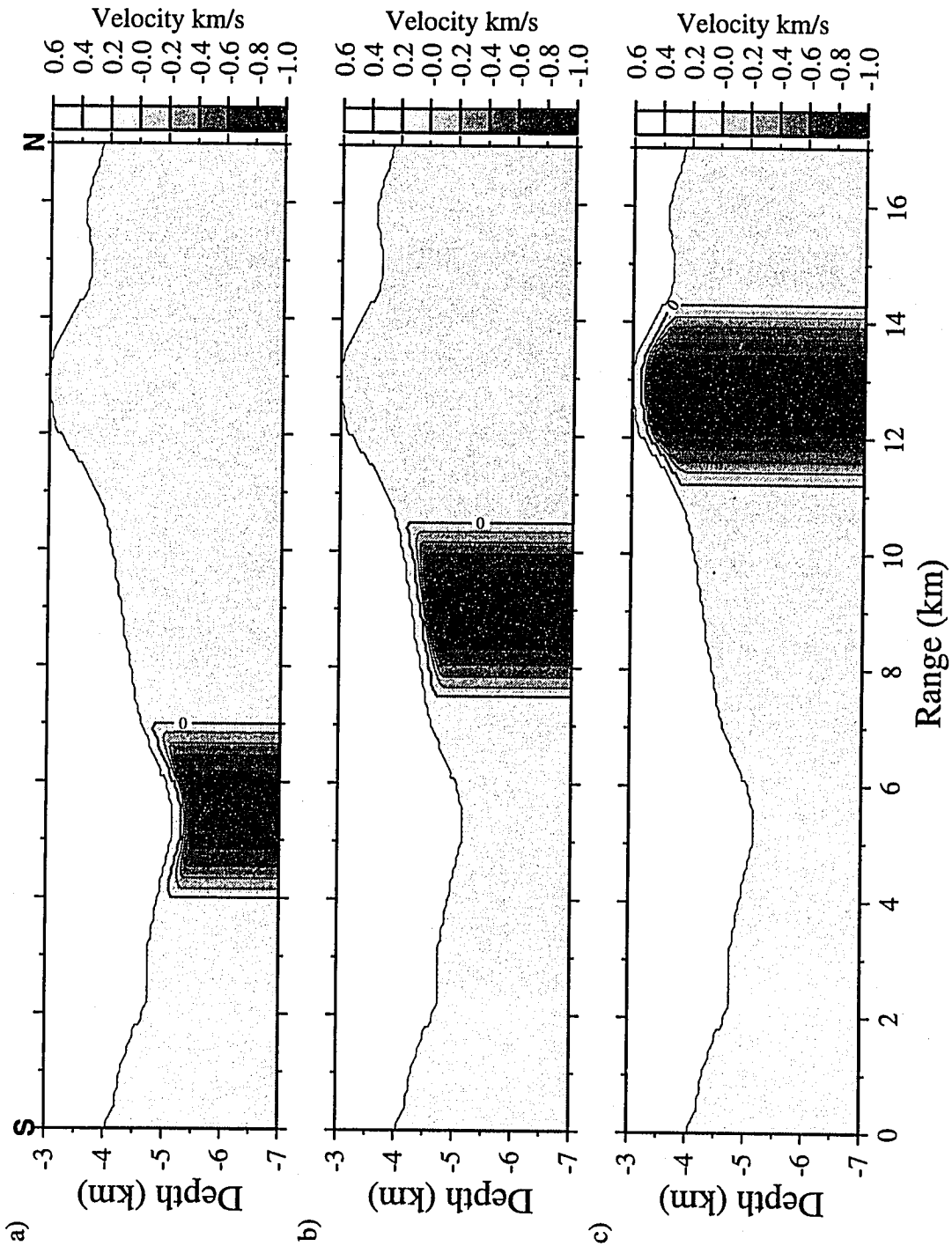
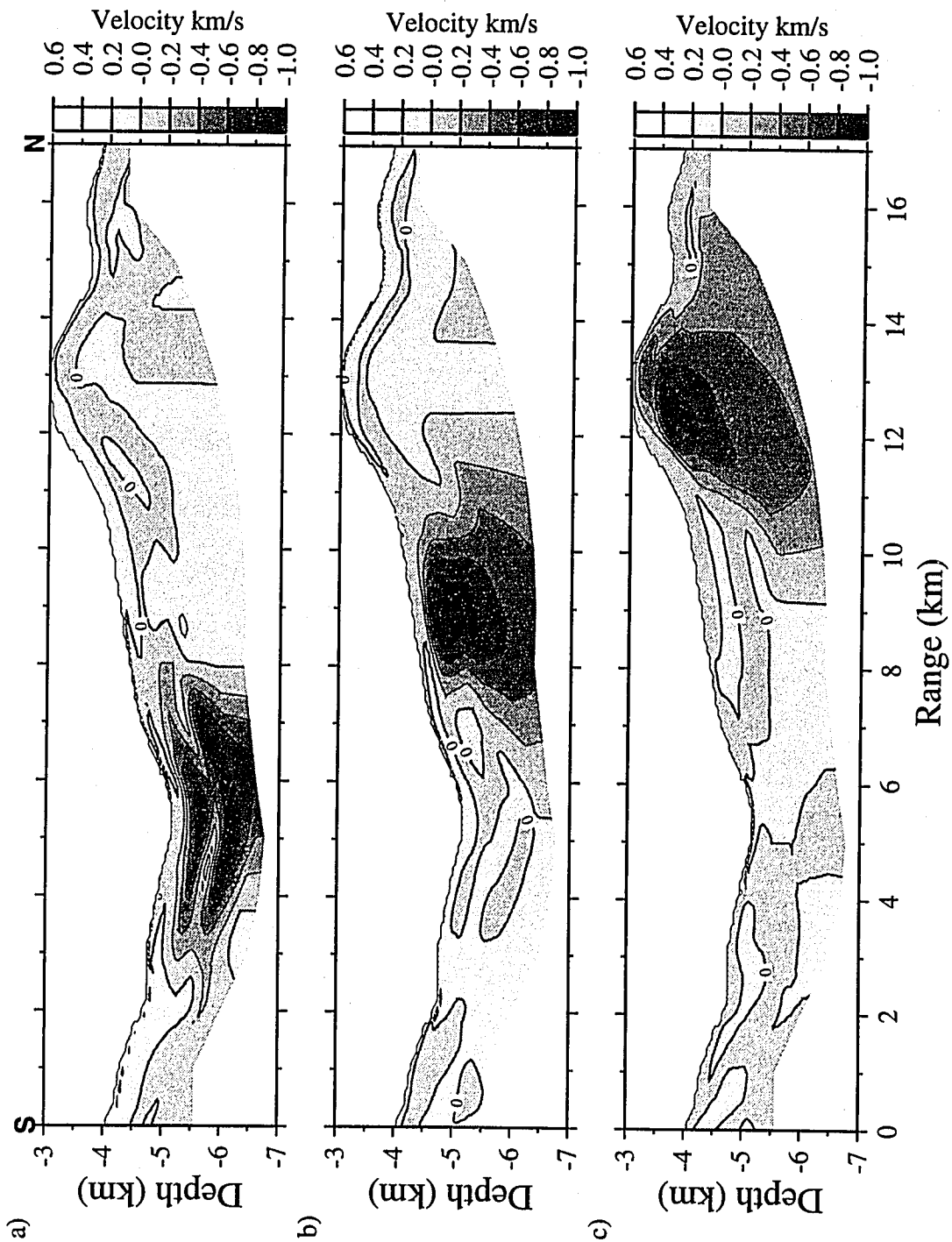


Figure 3.6 Iterative damped least-squares inverse results from noise-free data using the same parameterization scheme, penalty function weighting, and source/receiver pairing and geometry as the real inverse. The results of trying to resolve the structures in figure 3.5 are: a) for the valley, b) for the incline, and c) for the hill.



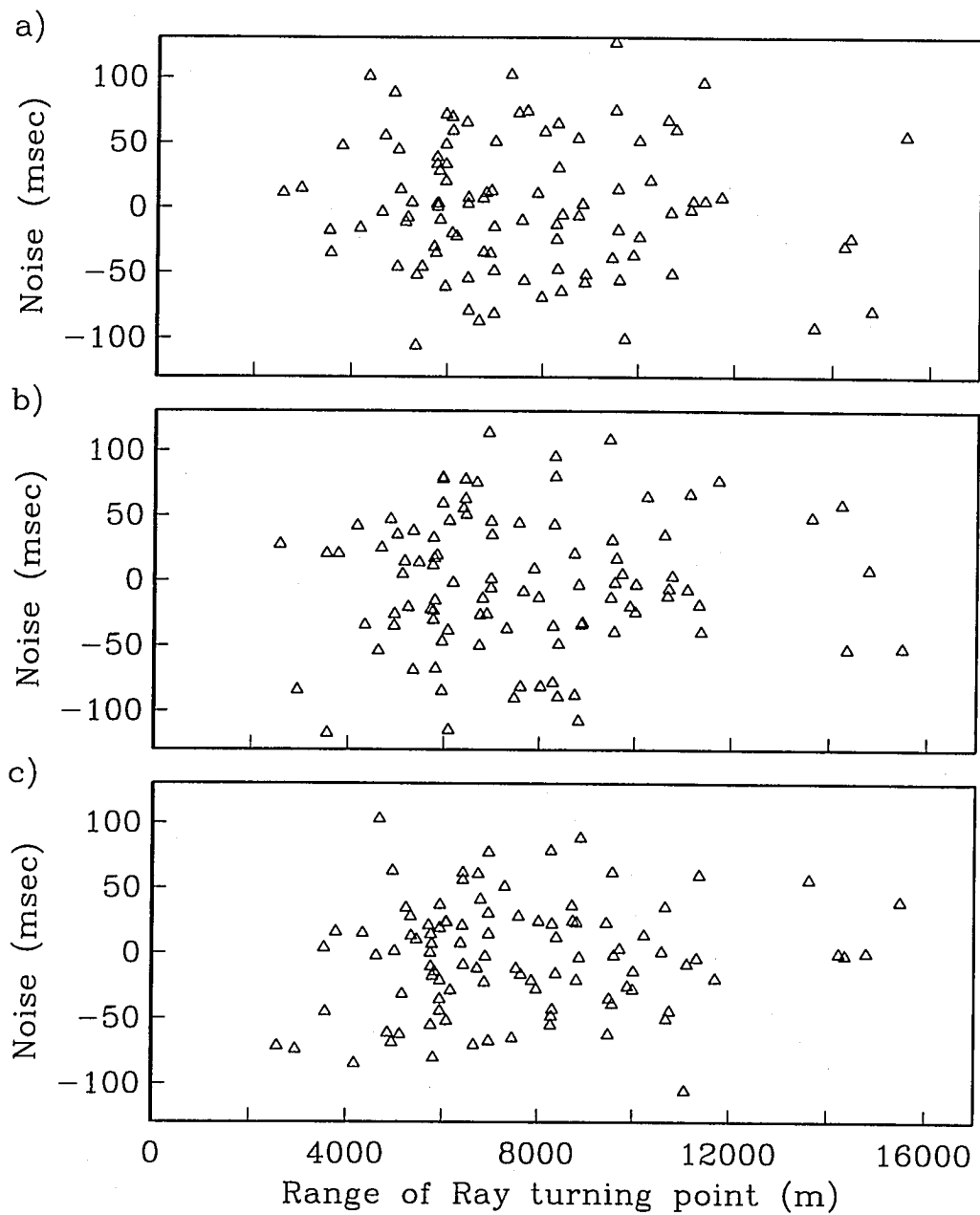
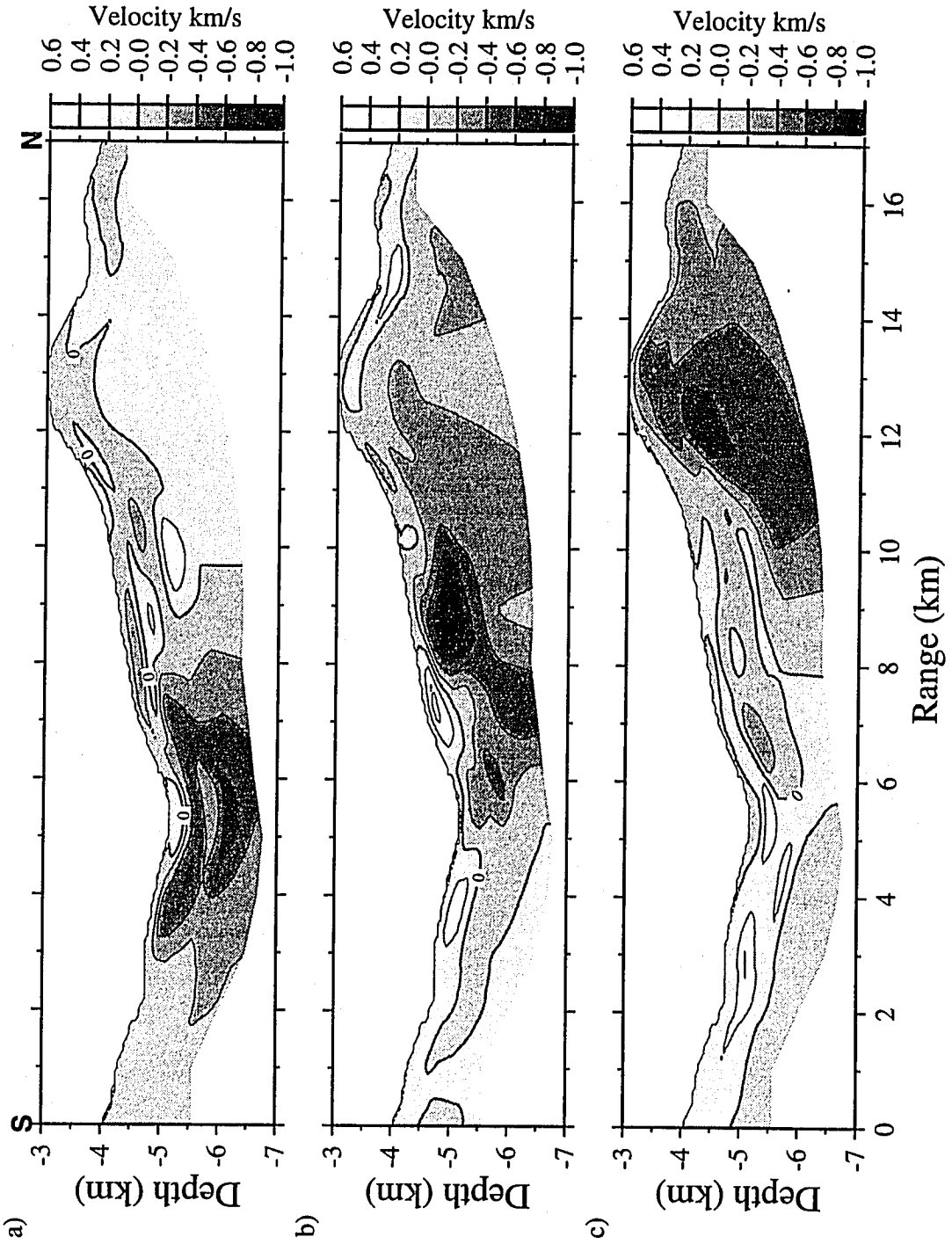


Figure 3.7 Normally distributed noise with zero mean and 50 msec standard deviation as a function of the range of the ray turning point. The noise a), b), and c) is added to the noise-free synthetic data for the valley, incline, and hill, respectively.

Figure 3.8 Iterative damped least-squares inverse results from noisy data using the same parameterization scheme, penalty function weighting, and source/receiver pairing and geometry as the real inverse. The normally distributed, zero mean, 50 msec RMS, noise from figure 3.7 is added to noise-free data to try to resolve the structures in figure 3.5. The results are: a) for the valley, b) for the incline, and c) for the hill.



CHAPTER 4

Results and Discussion

4.1 Introduction

The primary purpose of our seismic refraction survey is to characterize the geologic structure of the Hess Deep rift valley. Preliminary analysis [Wiggins *et al.*, 1992] showing anomalously high surficial velocities and densities in the intra-rift ridge provided the ODP Leg 147 group with additional data supporting their decision to drill for lower plutonics (gabbro) at the intra-rift ridge. Although they were only able to drill approximately 150 meters into the intra-rift ridge at site 894, the ODP group did recover gabbroic rocks with a high, average bulk density of $2.92 \pm 0.09 \text{ g/cm}^3$ and a fast, mean P-wave velocity of $6587 \pm 564 \text{ m/s}$, [Gillis *et al.*, 1993]. Further processing of the seismic refraction data provides a detailed velocity model of the substructure. The addition of the geophysical data to the bathymetric and petrological data is used to help constrain the possible structural models of the rift valley. The following is a discussion of the two-dimensional velocity model of the Hess Deep and corresponding geologic interpretations.

4.2 Iterative Stopping Point

The iterative damped least-squares inverse described in the previous chapter is used with the west line travel time data to solve for a two-dimensional cross-rift model of the substructure velocity field. The one-dimensional Hess Deep velocity model (figure 3.2) "hung" from the bathymetry is the starting model. The RMS travel time data residuals for the 98 rays traced through the reference velocity model is approximately 100 msec. The iterative process produces a set of successive models. Deciding which

model is best is a trade-off between the amount of model structure and the magnitude of data residuals. As model length increases, data residuals decrease. The spatial resolution of the model structure is limited to approximately 1 km horizontally with the choice of parameterization and instrument spacing; whereas, the noise in the data and the inability to model the substructure exactly limits the reduction of residuals to approximately 50 ms. Figure 4.1 is a plot of model length weighted by its expected uncertainty versus the corresponding data residual weighted by their expected uncertainties for a few independent iterative inverses. The plus (+) curve shows our first attempt with fairly large step sizes ($\sim \pm 1000$ m/s velocity model perturbations). The undesirable characteristic of increasing data residuals with increasing model structure results from nonlinearity caused by the topographic geometry of the valley across the Deep (see chapter 5). Taking much smaller steps ($\sim \pm 50$ m/s velocity perturbations) we avoid this nonlinearity effect as shown by the initially smooth asterisk (*) curve. The smooth descent of the data residuals with increasing model structure comes at the price of an increase in the number of iterations and consequently, an increase in the computation time. The model structure, or length, can be considered to consist of both spatial and magnitude terms. With the slow descent iterative method, the spatial boundaries of the velocity perturbations are resolved during the first few iterations. Later iterations do not change the position of the high/low velocity perturbations, just their respective amplitudes. As the iterations continue, even smaller model perturbations are needed to keep the problem linear. With the amount of model structure increasing with each iteration, ray tracing difficulties arise due to triplications and caustics. This is especially true in the valley where weak velocity gradients prevail. The effect can be seen in figure 4.1 where increased data residuals appear near the upper end of the asterisk curve. The forward problem ray tracer finds different branches of the triplication between consecutive iterations. In addition, some data are

lost (ray paths cannot be found) during later iterations as the model becomes structurally complex. We choose a solution at the 45th iteration on the asterisk curve that is represented by the diamond in figure 4.1. We have experimented with smaller steps which lessened the ray tracing problems, but no additional information on the geologic structure can be interpreted. The triangles of figure 4.1 represent trial modifications of the final model (diamond) in which the small scale features (high wave number) are partially filtered out from the final model to see if these features are artifacts of the iterative process. In both cases, removing the small scale structure decreases the model length while increasing the data residuals. The data residuals from the modified models are greater than the iterative (asterisk) data residuals for the same model length confirming that the iterative process does a better job of minimize the model length and data residuals. The same iterative process with a different starting model produces similar results. The curve indicated by circles in figure 4.1 results from starting with a model that is uniformly 500 m/s faster than the Hess Deep one-dimensional velocity model. Structurally, the results are the same as for the final model. The same high/low velocity perturbation regions are resolved to approximately the same amplitude. However, as expected, areas that are poorly resolved because of inadequate ray geometry/coverage (ie. the north and south edges of the model) do not correlate well because of the different starting models. Figure 4.2 shows the sum of the weighted model length and weighted data residuals (the penalty function/equation 3.9) versus iteration number. Minimizing the penalty function while assuring that most (> 90%) of the data (rays) are not lost from increased model structure yields the solution to the iterative inverse. The data rms residual from the final model is reduced to approximately 48 msec. Figure 4.3 shows the distribution of travel time residuals with respect to the range of the turning point of the ray. The residuals are fairly well scattered, but do have larger values in the valley region (4-8 km range) where higher levels of

nonlinearity persist (see Chapter 5).

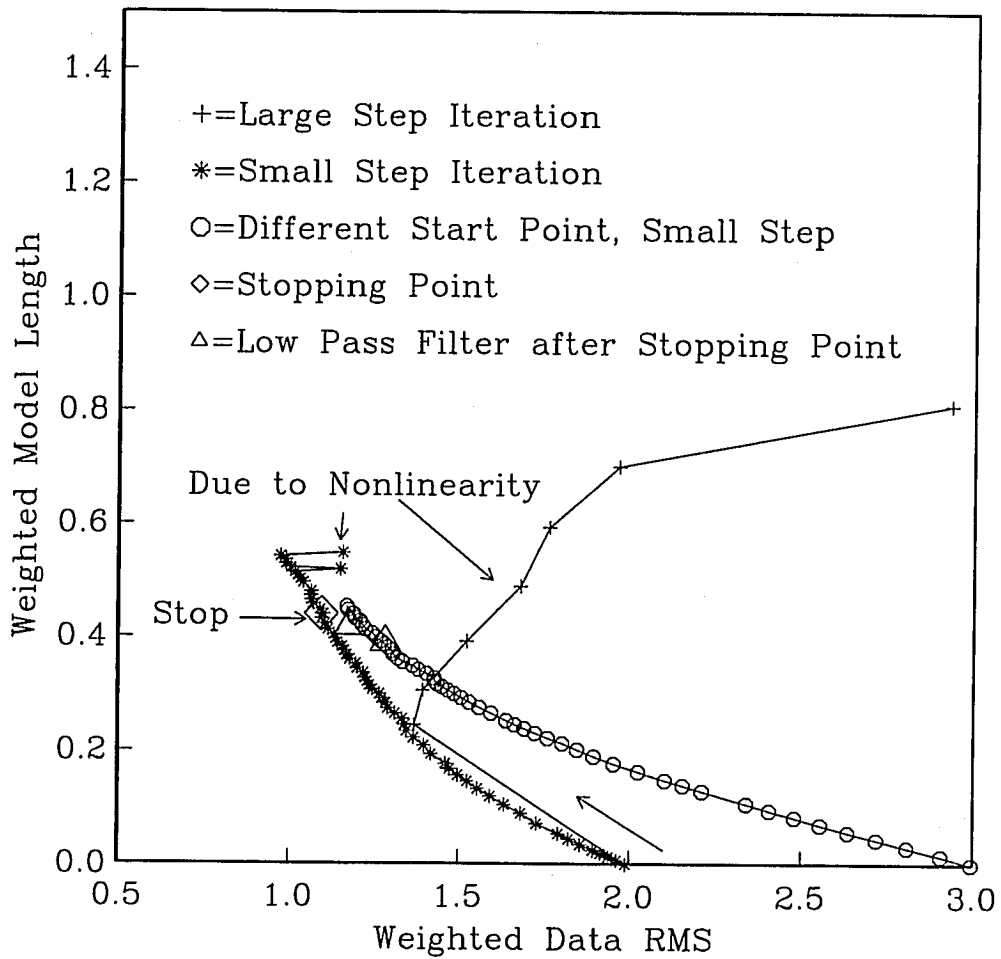


Figure 4.1 Trade-off between weighted data residuals and weighted model length for iterative damped least-squares inverse for different step sizes, starting models, and stopping points. All three iterative curves start at 0 model length and increase structure with each iteration.

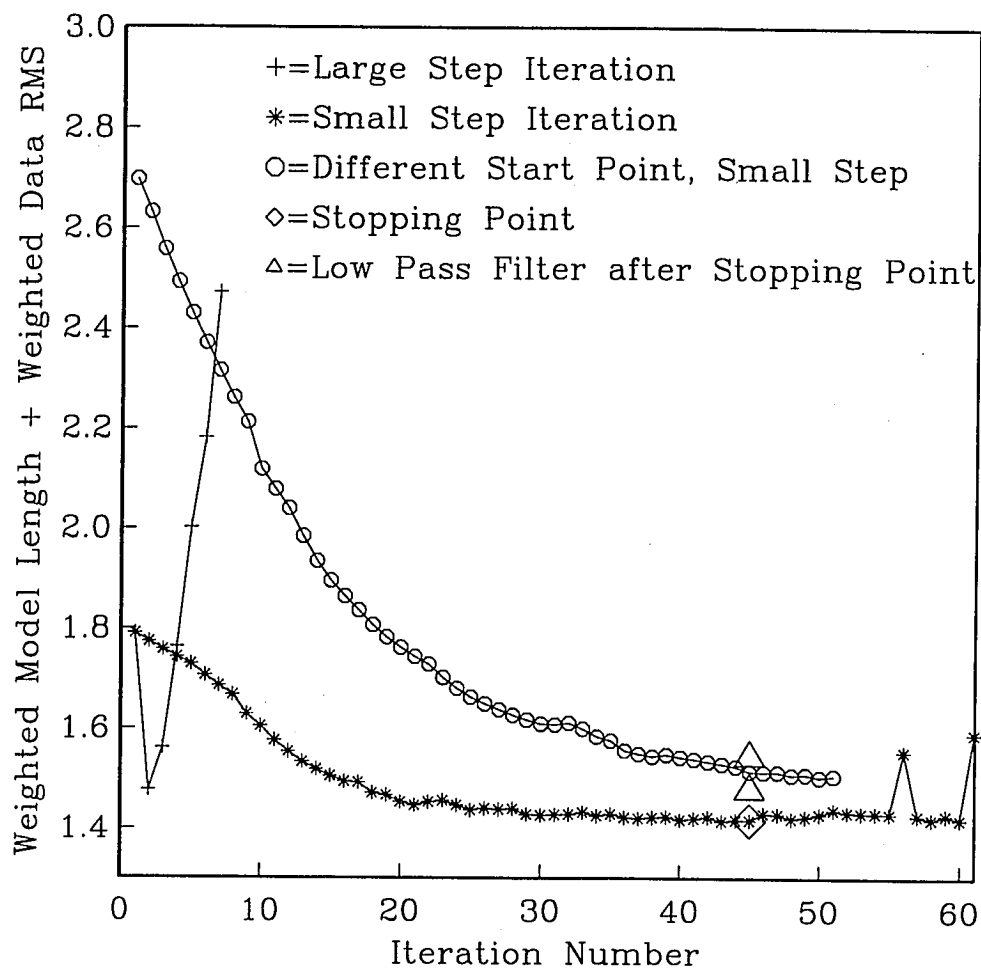


Figure 4.2 The sum of the weighted data residuals and weighted model length (penalty function) versus iteration for iterative damped least-squares inverse for different step sizes, starting models, and stopping points. Minimization of the penalty function yields the final solution.

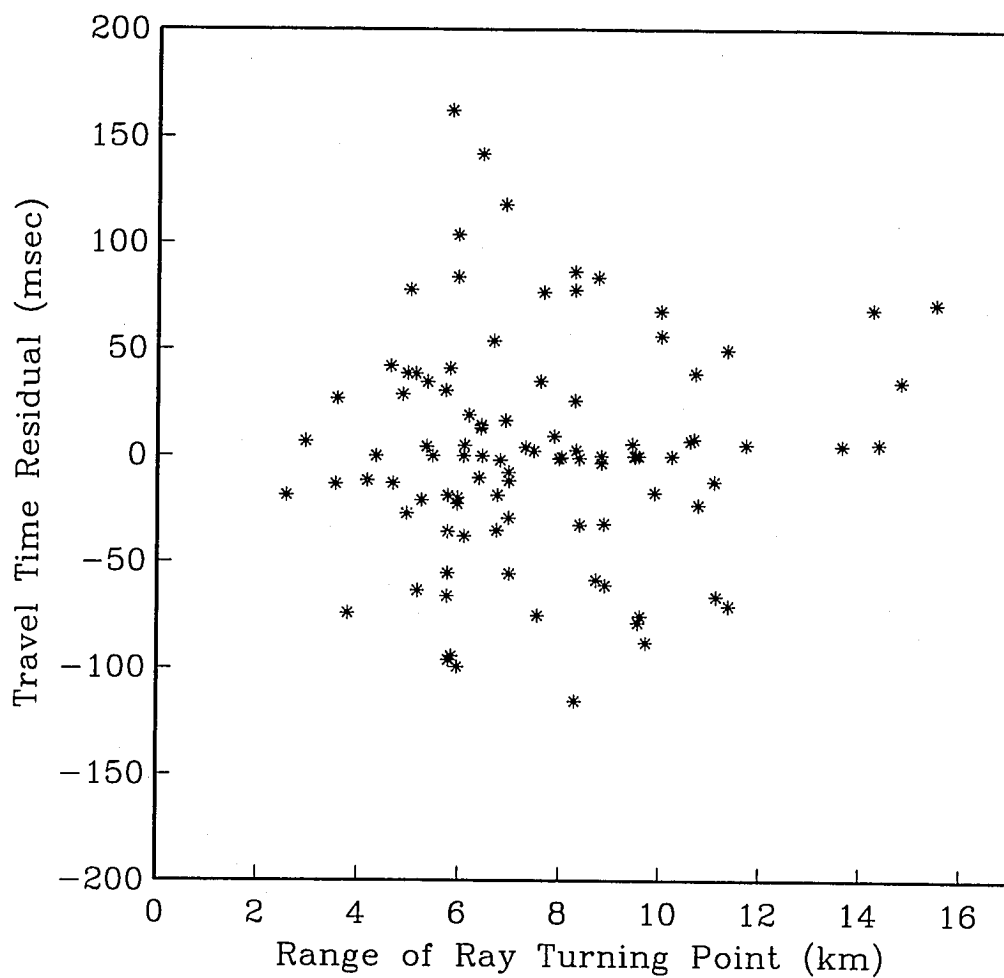


Figure 4.3 Travel time data residuals as a function of range of ray turning point. The distribution is well scattered with large values corresponding to the valley region (4-8 km range) where higher levels of nonlinearity persist (see Chapter 5).

4.3 Hess Deep Velocity Model

The results of the inverse are presented in figure 4.4. Figure 4.4a is a plot of the Hess Deep one-dimensional, depth dependent, reference model along with the initial ray paths traced through the unperturbed structure. The cumulative model perturbation output from the iterative inverse procedure is used to produce figure 4.4b. The perturbation plot illustrates that a given region of perturbation is anomalously faster or slower than the reference model. The reference model is constructed to be similar to typical, young, fast-spread, oceanic crust having the same velocity at a given depth independent of range; therefore, the perturbed regions are considered to be areas different in lithology and/or structure (ie. porosity/fracture) from typical layered oceanic crust. The range of the perturbations is approximately 1300 m/s to -1100 m/s. Figure 4.4c is a plot of the sum of the reference model and the perturbations along with the ray paths traced through the final model. It should be noted that the velocities in the final map are expected to be lower than those observed in core or dredge rock samples due to large and small scale fracturing, and averaging over long ray paths. The ray path coverage and geometry dictates the model resolution. Many near-perpendicular crossing rays have the ability to resolve small scale structure. However, given a fixed source/receiver spacing, it may be physically impossible to sample some regions. For example, beneath the north side of the valley, between 5.5 and 7.5 km range, the velocity gradient is weak ($dv/dz < 1$) and the rays refract away from sampling the area (figure 4.4c). This is a typical problem of trying to sample low velocity regions [e.g., *Toomey et al.*, 1994]. The deeper parts of figures 4.4b and 4.4c have been removed because of lack of data (rays) sampling.

The mathematically rigorous iterative inverse method requires a long period of initial set up, testing, and running to produce reliable results. Because ODP Leg 147 cruise followed our seismic refraction experiment by only 6 months, it was imperative

that we produce a velocity model of the substructure quickly to help with constraining the location of the drill sites. A forward-modeling, interactive, ray tracing program, (*MacRay*: Luetgert [1992]) was used to quickly derive a preliminary two-dimensional velocity model of the Hess Deep. Results from the ray tracing are used as an independent check on the damped least-squares inversion. The same one-dimensional velocity model of young EPR crust discussed in chapter 3 [Vera *et al.*, 1990] was used as a starting model. However, instead of holding the depths constant and varying the velocities at the layer interfaces, as in the iterative damped least-squares inverse, the velocities at the interfaces were held constant and the depths were interactively moved with the mouse cursor to minimize the data misfit. This type of procedure violates the linearity assumption due to the large ray path changes, but produces reasonable results within a relatively short time period. Figure 4.5b shows the results of the *MacRay* forward-modeling procedure. It is more instructive to compare the change in the velocity than the resulting velocity value at a given location because perturbation plots have more structure than the final velocity model plots. Some of the main characteristics of the damped least-squares inverse velocity perturbation plot (figure 4.5a) are reproduced by the *MacRay* forward-modeling (figure 4.5b). In both models, anomalously slow regions are shown beneath the valley; whereas, high velocity regions are resolved beneath and on the south flank of the intra-rift ridge. Even the small scale, fast regions near the surface at approximately 8 km range and approximately 5 km below sea level (bsl) at approximately 10 km range are found by the *MacRay* forward-modeling procedure. In general, however, *MacRay* did not reproduce the small scale features and low velocity (weak vertical velocity gradient) zones found by the iterative damped least-squares inverse because the *MacRay* model was biased to increase velocity with depth using a small amount of horizontal variability. In addition, the results of iterative damped least-squares method are independent of starting point. Figure 4.5c shows the

results starting with a model that is uniformly 500 m/s faster than the Hess Deep one-dimensional reference model. The perturbation plot is produced from the difference between the final velocity model and the same reference model used for figures 4.5a and 4.5b so that a comparison can be made. In light of geologic interpretation, figure 4.5c is identical to figure 4.5a.

Figure 4.4 Iterative damped least-squares inverse results: a) Reference model generated from Hess Deep 1-D velocity profile (figure 3.2) "hung" from the bathymetry creating iso-velocity lines that follow the sea floor. Also shown are the initial ray paths traced through the reference model. b) Resulting cumulative perturbation map from iterative inverse. c) Final velocity model is the perturbations added to the reference model. Notice the change in the ray paths from figure 4.4a. The density of ray coverage becomes less dense in some regions due to low velocity zones (weak velocity gradients).

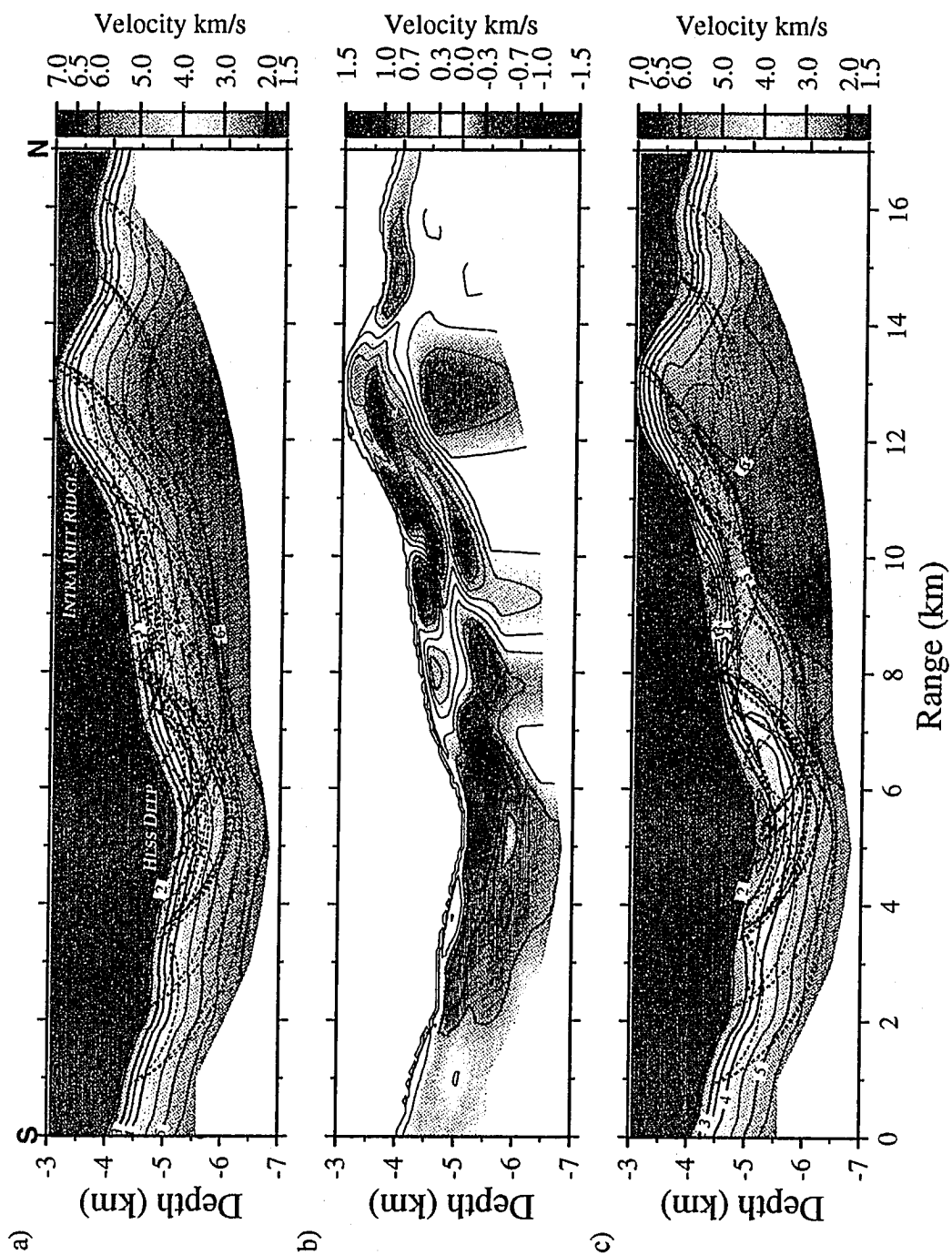
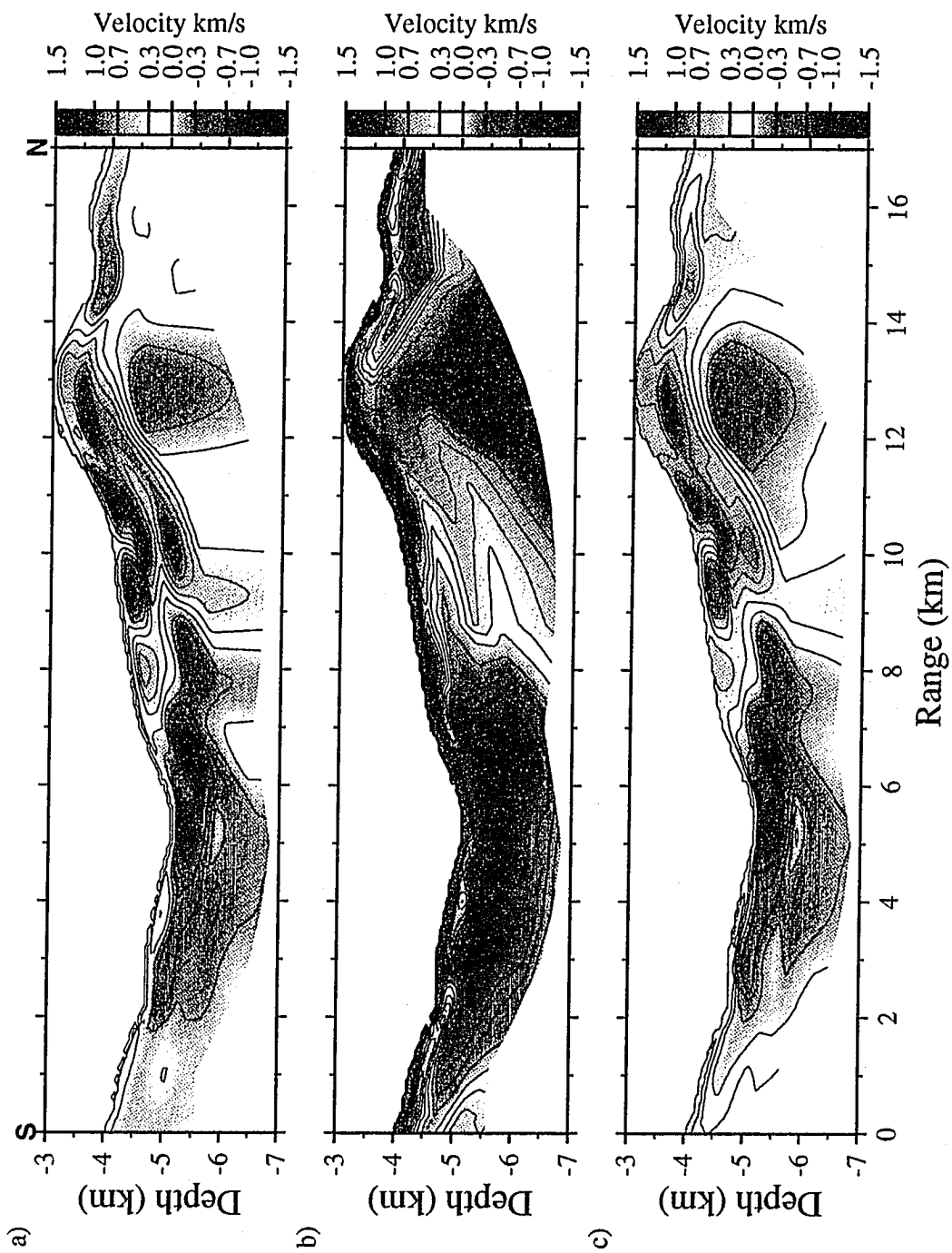


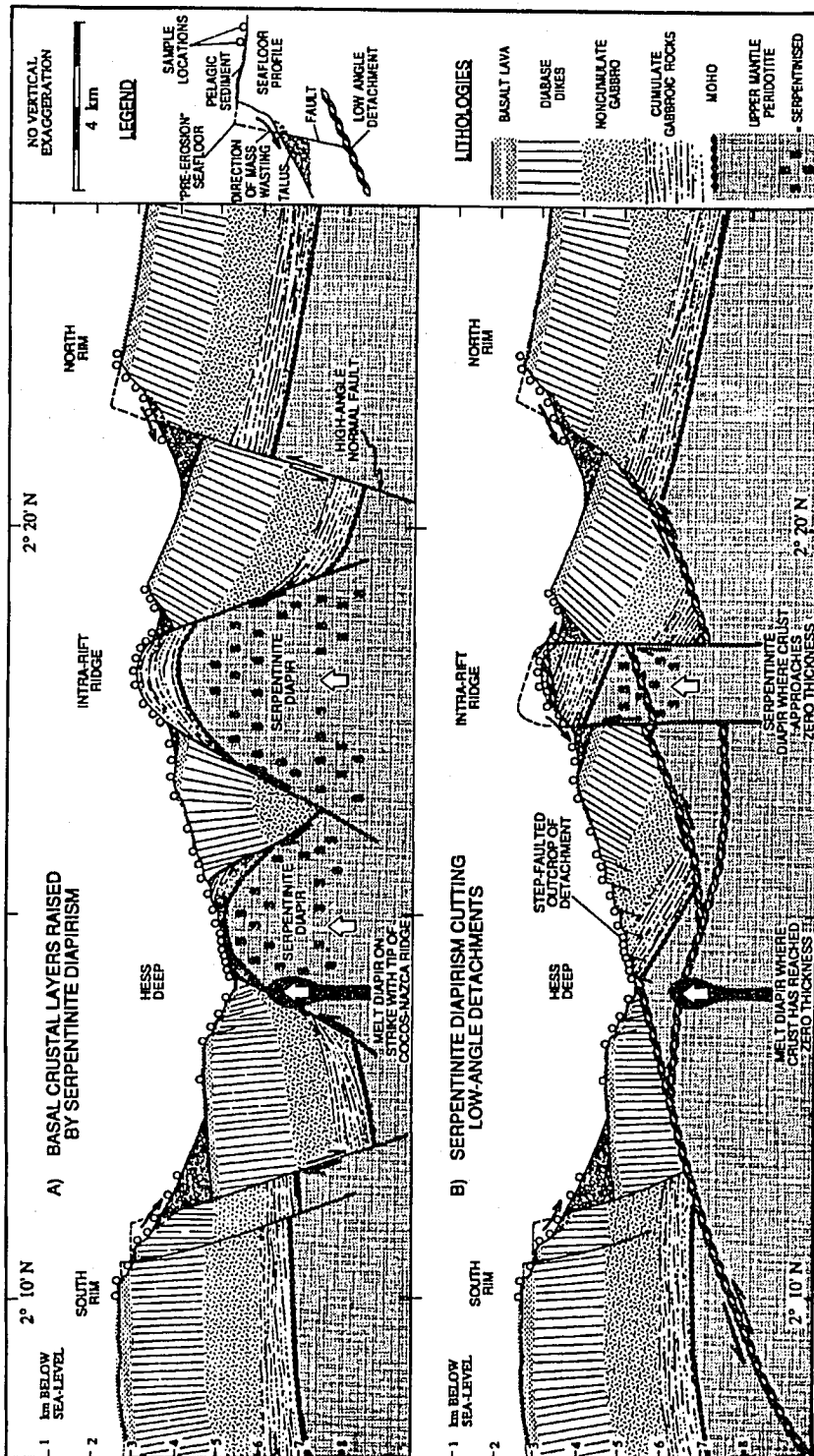
Figure 4.5 Comparison of Inverse Results: a) Iterative damped least-squares inverse perturbation results (same as figure 4.4b). b) *MacRay* interactive forward-modeling procedure perturbation results starting with the same Hess Deep 1-D reference model use for the iterative damped least-squares method. Large scale features (i.e. slow velocity in the valley and fast velocity in the intra-rift ridge) are similar to iterative damped least-squares inverse in figure 4.5a. The plot was generated by subtracting the reference model from the final model. c) Iterative damped least-squares inverse perturbation results starting with a reference model that is uniformly 500 m/s faster than the Hess Deep 1-D model. The plot was generated by subtracting the Hess Deep 1-D model from the final velocity model so that a comparison to figure 4.5a can be made. The similarity to figure 4.5a indicates that the results of this method are independent of starting point.



4.4 Structural Interpretation

The objective of a seismic refraction experiment is to produce a velocity model of the sampled subsurface rocks. Figure 4.4 shows this result. But the primary question is: what do these velocities and/or perturbations represent? What does the subsurface velocity structure tell us about the unusual lower crustal rock exposures in the Hess Deep rift valley? *Francheteau et al.*, [1990] used data from SEABeam bathymetry, dredge samples, and rock samples gathered and viewed with a submersible (see figure 1.4) to produce interpretative sketches of two possible models of the subsurface geology. Two north/south cross-section models are presented in figure 4.6. The shallow structure of two models are essentially the same south of the Deep and north of the intra-rift ridge. The model in the top panel emphasizes high-angle normal faulting during extension with serpentinization of peridotite causing diapiric uplift and exposure of the lower crustal gabbros. The large amounts of cataclastic and brecciated rocks along with the visual observations of serpentine on the flanks of the intra-rift ridge support this model. On the other hand, the mechanism of exposure for the lower panel model is low angle detachment where the upper crust has been stripped away. The topographic asymmetry of the valley along with cataclastic rocks and mixing of lithological units on the slope north of the Deep defend the second model. The seismic velocity data is combined with the geologic and bathymetric data to form two other possible models addressing the mechanisms described in figure 4.6.

Figure 4.6 Sketchs of the Hess Deep, cross-rift, geologic structural models from *Francheteau et al.*, [1990]. The top panel depicts high angle normal faulting with serpentinization of peridotite exposing lower crustal/upper mantle rock as the dominate mechanisms. The bottom panel shows low angle detachment faulting with minor serpentinization as the primary forces of plutonic exposure.



In order to form a geologic structural model we need to constrain the lithological thicknesses of fast-spread EPR crust. Typical oceanic crust is considered to be layered top to bottom: sediments, extrusive lava basalts, intrusive dikes (dolerite), and gabbros (noncumulate and cumulate). Beneath the gabbros is the upper mantle peridotite. Because the Hess Deep rift valley region is relatively young (~ 1 MA), we assume that normal layering of sediment is thinner than we can resolve. In a follow-up paper, *Francheteau et al.*, [1992] concluded from examination of the walls of Hess Deep with the submersible *Nautila* that the extrusives are 100 - 200 meters thick and that the sheeted dikes are at most 1200 meters thick. We choose a conservative 1200 meter thick Layer 2 (basalt and diabase dikes) for our model. Geophysical results from experiments conducted near the Hess Deep [*Neprochnov et al.*, 1980 and *Zonenshain et al.*, 1980] support a model Layer 3 (gabbro) thickness of 3 - 3.5 km. Typical unruptured oceanic crust layered in this way increases velocity with depth, first very quickly (strong velocity gradient) then after approximately 500 meters the gradient decreases to approximately 1 sec^{-1} (see figure 3.2). There are many factors which influence sound velocity in rock: lithology, pressure from over-lying rock, porosity, fracturing, alteration, and mineral anisotropy. Because the rock units/blocks of the Hess Deep valley are jumbled, mixed, and rotated and our seismic array is a cross-axis line, we cannot resolve anisotropic features. Mylonitic zones generally have small (<50 meters) widths but can be inferred because they are discontinuities bounding larger blocks that can be resolved. High porosity mainly occurs in extrusives and shallow dikes and decreases with depth beneath the seafloor due to the pressure of the over-lying rock closing the voids and fractures. Geologic structural models are concerned with lithological locations, fracturing/faults and alterations related to dynamic forces (ie. serpentinization of peridotite, mylonitic zones, brecciated rocks). The velocity perturbation plot is used instead of the velocity plot during geological interpretation

because it shows more structure and provides a means of removing the velocity dependence on depth beneath the seafloor, singling out lithological differences. At a given depth, an anomalous velocity value indicates the presence of rock originating at a different depth and/or alteration of the rock. Negative velocity perturbations can arise by covering originally shallow crust with faster rock, introducing large amounts of fracturing filled with sediment and/or water entrainment, accumulating breccia or talus on the seafloor, altering upper mantle peridotite into serpentinite from interaction with sea water transmitted via cracks in the over-lying crust, and the introduction of new melt. Positive velocity perturbations are associated with plutonic rocks (gabbros/deep diabase dikes) that are brought to shallower depths as a result of low-angle faults stripping away of upper crust or uplifting buoyancy forces created by serpentinization of peridotite.

Using these criteria, we can interpret the geological significance of the velocity perturbations from the inversion. Figure 4.7 shows both a sketch of the possible present day geologic structure addressing the high-angle normal faulting mechanism from the top panel of figure 4.6 and the velocity perturbation plot (same as figure 4.4b) used for the interpretation. In addition, to help constrain the geological interpretation of the velocity perturbations, the petrological results from *Francheteau et al.*, [1990] (see figure 1.5a) are presented as symbols above the bathymetry in figure 4.7b. The seismic data constrains the geologic structure from a few kilometers south of the Deep to a few kilometers north of the intra-rift ridge. Because the refraction survey adds no additional constraints to the northern and southern ends of the cross-section, structure similar to the *Francheteau et al.*, [1990] models is assumed. Although the rift valley is three-dimensional with respect to rock movement, observations of *in-situ* dikes show no preferential tilt and are nearly vertical [*Francheteau et al.*, 1992]; therefore, rock movement is assumed to be across axis and vertical producing a balanced structural

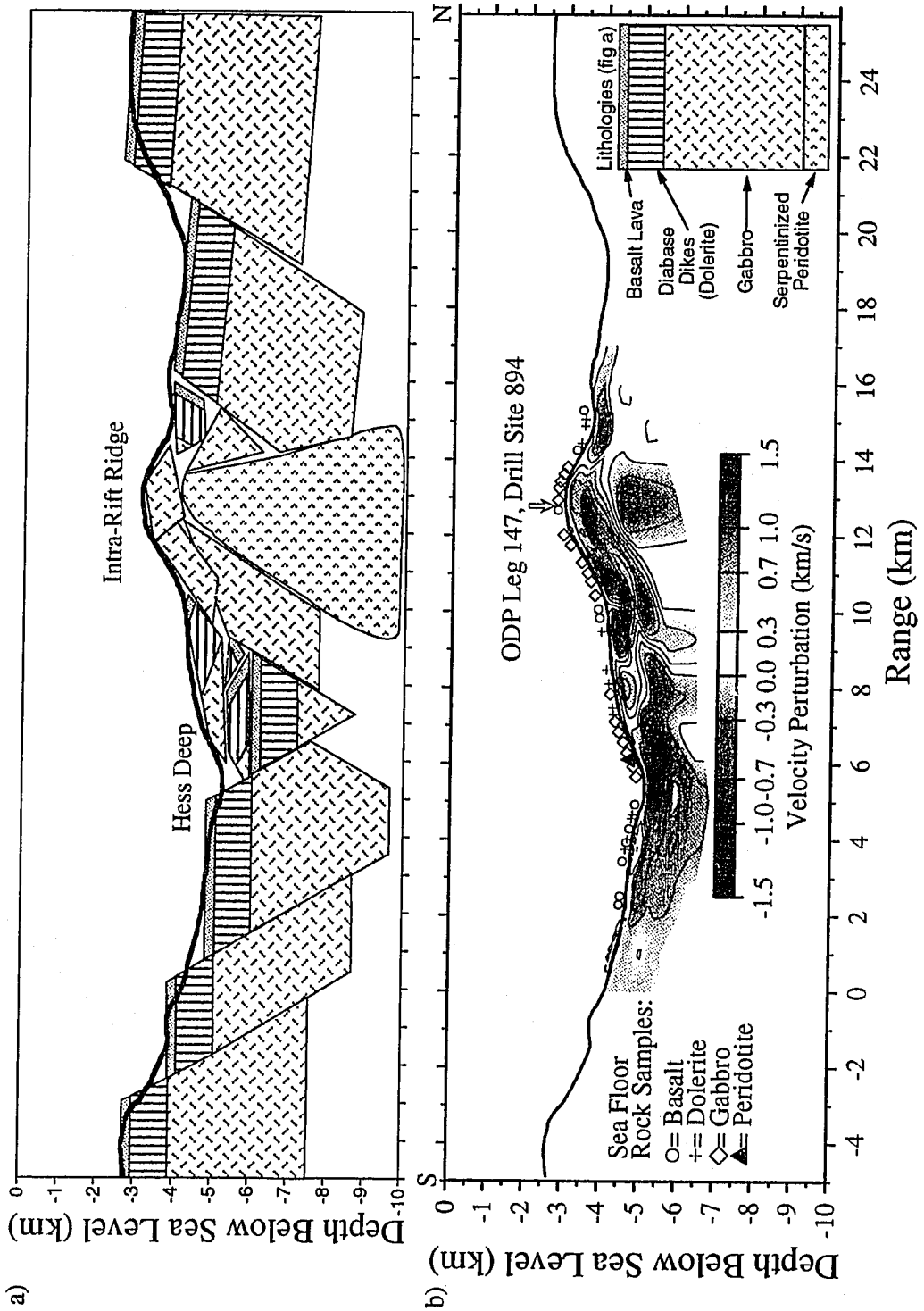
cross-section. Even though tectonic forces deform and round block units, produce accumulation of talus on the sea floor, and line block boundaries with mylonitic zones, the blocks in figure 4.7a are only broken in large units and are not deformed nor eroded, preserving their original volume. The region beneath the gabbros of the normally layered block units and the serpentinite diapir is upper mantle peridotite and may be serpentinitized to varying degrees.

One of the most intriguing geological questions of the Hess Deep area is why should high density/velocity, lower crustal rock be uplifted to form the intra-rift ridge? The feature beneath the intra-rift ridge at approximately 13 km range in figure 4.7b provides an answer to this question. The anomalously high velocity perturbation overlying a low velocity feature is considered to be gabbroic rock carried to the surface by a less dense/more buoyant, seismically slow serpentinite diapir. The gabbros observed, dredged, and cored on the intra-rift ridge concur with the resolved high velocity perturbation. In addition, paleomagnetic studies of the gabbros cored at ODP Site 894 show a 30-40° northward rotation of the gabbroic unit [MacLeod *et al.*, in press]. This is in agreement with the gabbroic block initially broken at 60° at 12-14 km range and is now tilted at approximately 20° from the horizon. The block units beneath the slope from 6-9 km range and 5-6 km below sea level corresponding to anomalous slow velocity are not considered intact rock units, but rather as broken up rubble from early stages of rifting. The shallow, negative velocity perturbation in the Deep at 5-6 km range is due to sediment and rubble fill; whereas, the general, large scale, anomalously slow region deeper is interpreted as a large amount of fracturing caused by the westward propagating tip of the Cocos-Nazca spreading center. The gentle slope from the Deep up to the base of the intra-rift ridge is inferred to be a broken slice of basalt, diabase dikes, and gabbro that slid down toward the valley. The fast region near the sea floor at 7-9 km range matches well with the diabase and gabbro samples observed

there. The anomalous slow region at 9-10 km is most likely fractured basalt and shallow diabase and talus accumulation. The slow zone north of the intra-rift ridge at approximately 14-16 km range is not interpreted as a complete block, but rather as well fractured basalt and dike material.

A proposed evolution of the geologic structural model in figure 4.7a is shown in figure 4.8. The initially unbroken model is 24 km long and has extended to approximately 31 km at present. Figure 4.8a shows the model during the early stages of tectonic extension in which high-angle normal faulting is the primary method of rock fracturing. Serpentinization of the upper mantle peridotite starts and is fueled by the introduction of sea water along the northern most fault. The lack of large amounts of magmatic intrusions at the Hess Deep implies that the upper mantle is sufficiently cool to serpentinize. Further extension creates more breaks in the crust and lowering of block units; whereas, increased serpentinization at 10 km range buoys up a relatively small block (figure 4.8b). Figure 4.8c chronologically precedes figure 4.7a and shows further breaking, sliding, rotating, and rising of rock units due to tectonic extension and serpentinization of peridotite. As in figure 4.7a, the blocks are kept whole without deformed rounded edges and some space between rock units are left void without fill to show the general movement/placement of the crust. Much smaller pieces could be used to produce a model with less voids, but that would be beyond the resolving capabilities of the seismic refraction data.

Figure 4.7 a) High-angle normal faulting structural cross-section interpreted from perturbation map and sea floor rock samples. Blocks have not been deformed nor eroded so that their original volume is preserved. It is left up to the reader to mentally round the corners of the blocks and to fill in the voids beneath the bathymetry with talus and between rock units with cataclastic and mylonitic zones. b) Velocity perturbation plot (same as figure 4.4b). Warm colors are anomalously fast; conversely, cool colors are anomalously slow. Regions can become fast if gabbros and/or deep diabase dikes are brought to shallower depths; whereas, slow regions are caused by serpentized peridotite at depth, fracturing with sediment and/or water entrainment, shallow crust being covered with rock, and the accumulation of brecciated rock or talus on the sea floor.



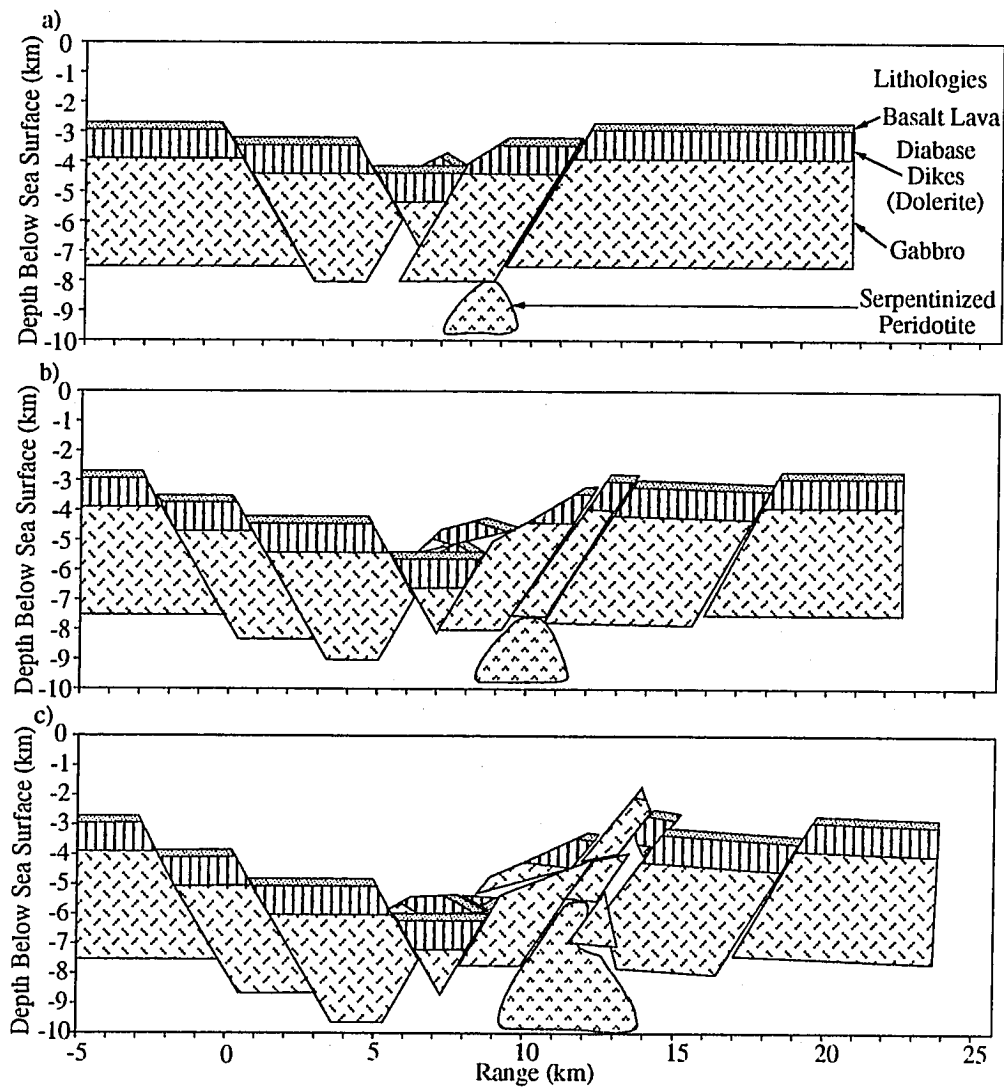


Figure 4.8 From a) to c) is the evolution of a proposed high-angle normal faulting geologic structural model preceding present-day figure 4.6a.

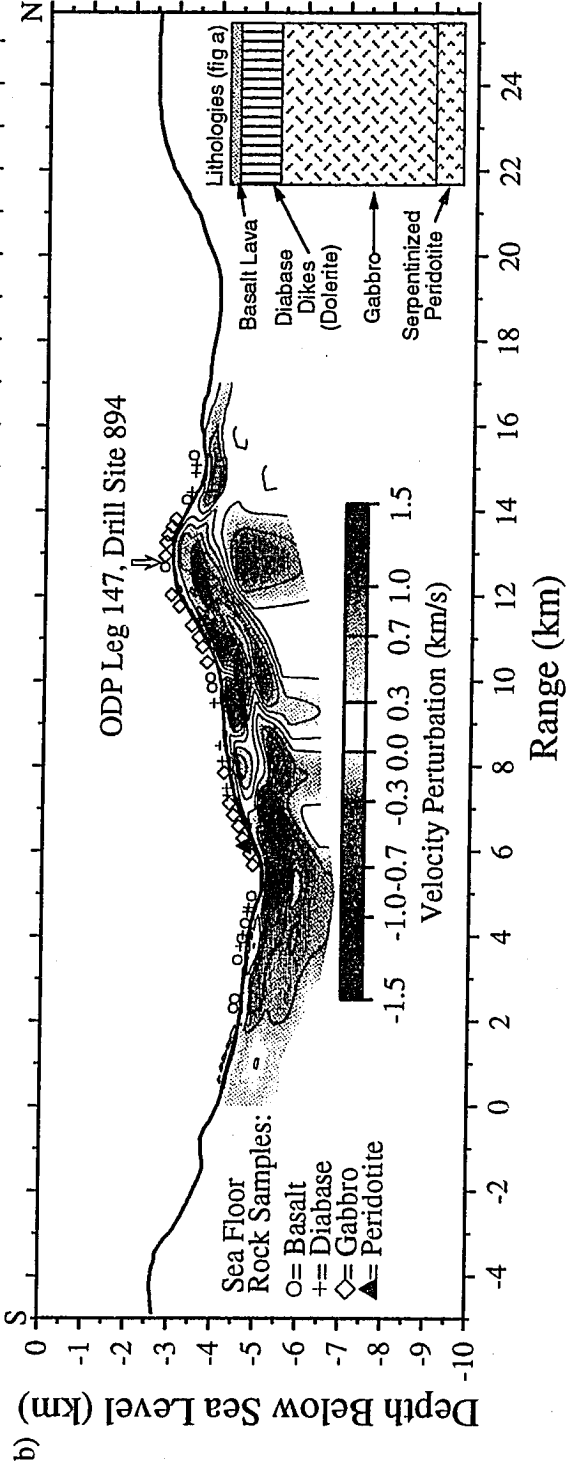
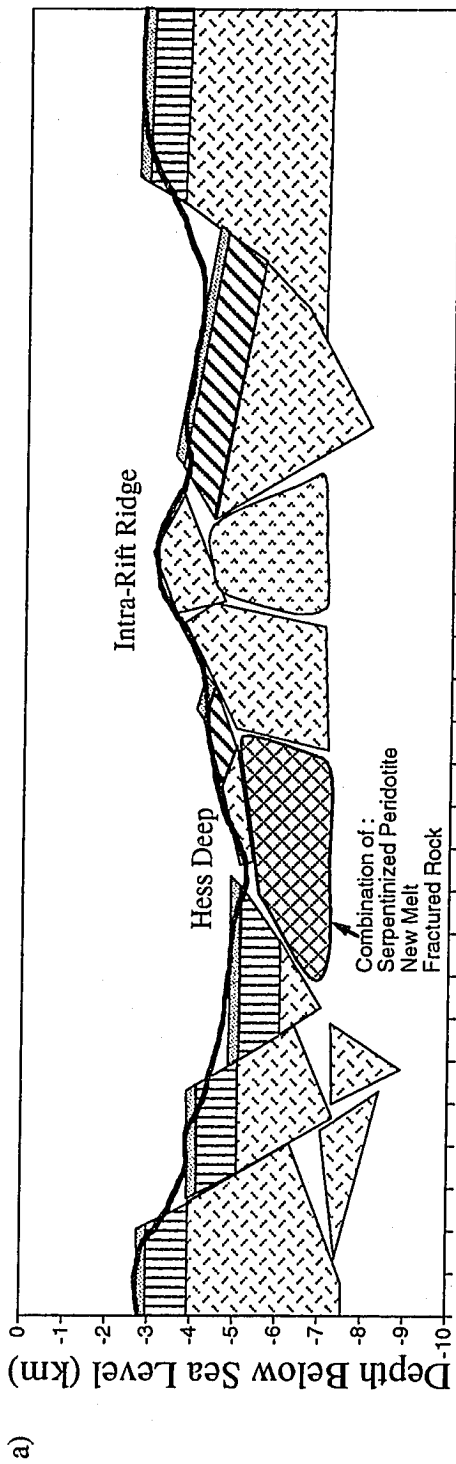
The preceding geologic model is a balanced cross-section addressing the high-angle normal faulting and serpentinization mechanisms of the model presented by *Francheteau et al.*, [1990] (top panel of figure 4.6). Although the geologic model fits the refraction data well, the evolution may be somewhat implausible. For example, the low-angle breaks and sliding of the blocks in the center of the model that are mainly due to gravitational forces may be reasonable for clays or sedimentary rocks, but are not very realistic for the higher shear strength oceanic crust without the aid of some tectonic mechanism. The lithological/seismic velocity relationships outlined above are again used to interpret the geological significance of velocity perturbations while addressing the low-angle detachment model of *Francheteau et al.*, [1990] (lower panel of figure 4.6).

Figure 4.9a is a geologic interpretation of the velocity perturbation plot (figure 4.9b) showing low-angle detachment faulting with serpentinite diapirism as the primary mechanisms of formation. Many of the lithological aspects of figure 4.9a are similar to the high-angle normal fault model of figure 4.7a because the same data is used for interpretation; however, the means by which the rocks arrived at their present locations is different. From south to north, the similarities include the blocks to the south of the Deep broken by high-angle faults, the slice of layer 2 and 3 (basalt, diabase dikes, and gabbro) forming the shallow structure of the slope from the Deep to the base of intra-rift ridge, the gabbroic blocks beneath the intra-rift ridge along with the uplifting serpentinite diapir, and the large blocks north of the intra-rift ridge. There are two main differences between the models of figure 4.7a and 4.9a. The first is the interpretation of the anomalously slow region beneath the valley of the Deep as serpentinized peridotite, new melt, and fractured rock instead of only highly fractured crustal rock. The other difference is the low-angle detachment faulting that rotated the block north of the intra-rift ridge and under-cut the blocks south of the Deep. The

serpentinite and melt beneath the deep provides a reasonable solution to the exposure of the observed surficial serpentinite outcrops and fresh lava flows on the floor of the Deep (figure 1.4). It should be noted that serpentinitization of peridotite occurs in varying degrees; therefore, the region beneath the Deep should not be interpreted as fully serpentinitized. Additionally, if the melt supply were copious, a conventional spreading ridge would result, as occurs east, along the Cocos-Nazca spreading center.

Figure 4.10 shows the proposed evolution of figure 4.9a. The initially unbroken model is 20 km long and extends to approximately 31 km in figure 4.9a. In figure 4.10a, initial extension breaks the crust by low-angle detachment faults that continue down into the upper mantle. High angle faults occur in the crust over-lying the detached block. The tip of the detached block breaks from the weight of above crust as the block rotates, tilting toward the north. The cracks in the crust provide pathways for the sea water to travel down to and interact with the upper mantle peridotite causing serpentinitization. Continued extension starts the stripping away of a thin section of basalt, diabase dikes, and gabbro as shown in figure 4.10b. Buoyancy forces from increased serpentinitization breaks the gabbroic section of the rotated block and initiates the uplift of the gabbroic block. The small block of gabbro that eventually forms the top of the intra-rift ridge is considered to partially erode during its ascent. In figure 4.10c, further extension and serpentinitization continues to uplift the gabbroic block and thin section of layers 2 and 3; whereas, the southern blocks broken at high-angles continue to drop. Finally, figure 4.9a follows as the present-day structure.

Figure 4.9 a) Low-angle detachment fault structural cross-section interpreted from perturbation map and sea floor rock samples. Blocks have not been deformed nor eroded to preserve their original volume except for the block at the top of the intra-rift ridge. It is left up to the reader to mentally round the corners of the blocks and to fill in the voids beneath the bathymetry with talus and between rock units with cataclastic and mylonitic zones. b) Velocity perturbation plot (same as figure 4.4b). Warm colors are anomalously fast; conversely, cool colors are anomalously slow. Regions can become fast if gabbros and/or deep diabase dikes are brought to shallower depths; whereas, slow regions are caused by serpentized peridotite at depth, fracturing with sediment and/or water entrainment, shallow crust being covered with rock, the accumulation of brecciated rock or talus on the sea floor, and new melt.



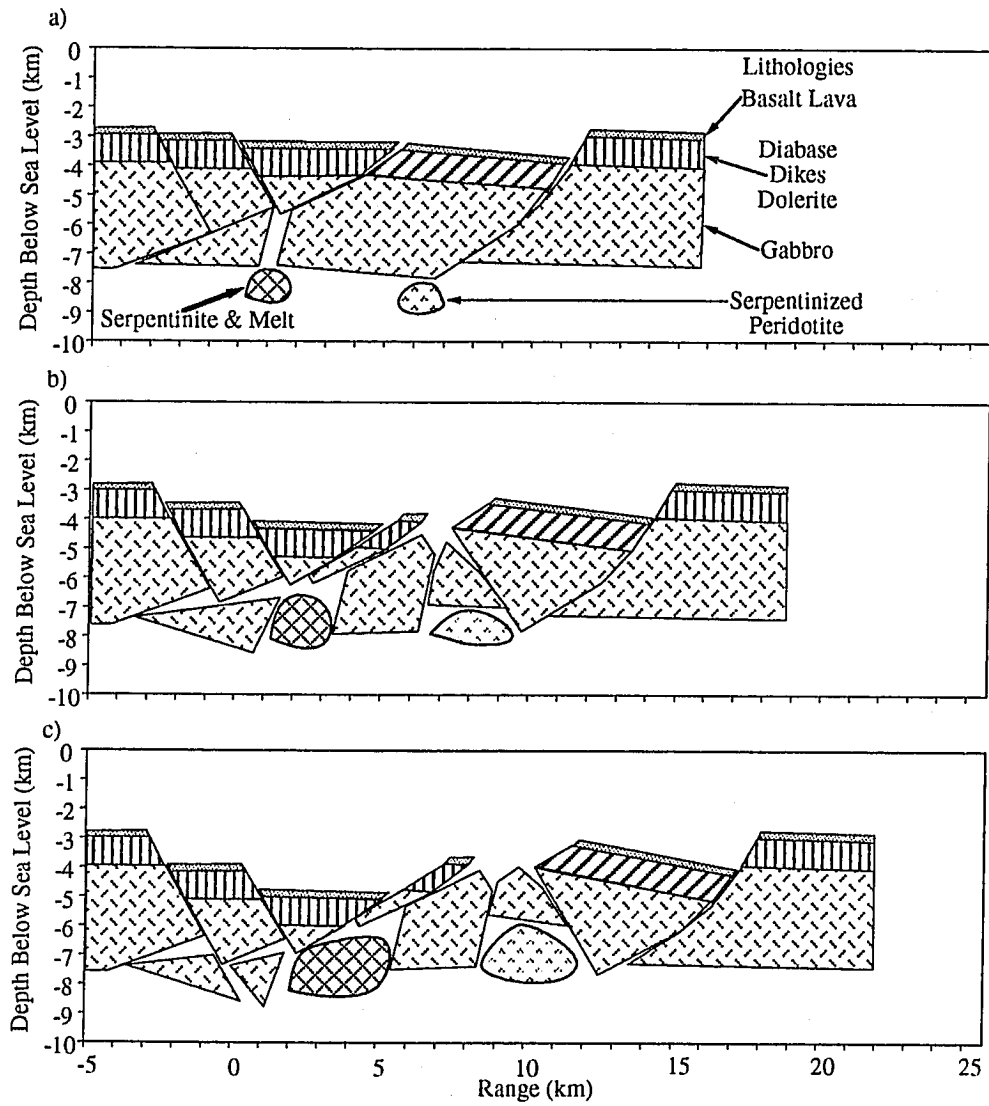


Figure 4.10 From a) to c) is the evolution of a proposed low-angle detachment faulting geologic structural model preceding present-day figure 4.8a.

4.5 Conclusion

Using the *MacRay* interactive forward-modeling procedure, preliminary velocity model results showing high surficial velocities beneath the intra-rift ridge support drilling gabbroic rock at ODP Leg 147 drill hole, 894. The more statistically rigorous iterative damped least-squares inverse method (chapter 3) produces a velocity model with more small scale structure and similar large scale features. The resulting perturbation plot provides a means of taking the depth dependence out of the velocity model, exposing lithological and structural differences. Two new geologic structural models of the Hess Deep rift valley are postulated from subsurface constraints provided by the velocity perturbation interpretation and surficial constraints given by the petrological and bathymetric data. Both models fit the seismic, petrological, and bathymetric data well; however, the low-angle detachment model (figures 4.9a and 4.10) has a more plausible evolution and is similar in some aspects to the *Francheteau et al.*, [1990] low-angle model. Data from the gravity survey and earthquake locations may provide more information to further constrain the possible models, but require additional processing.

The geologic models presented are a tradeoff in philosophies. Geophysicists who do not want to over-fit the data, produce smooth, simplified models; while, structural geologists produce complicated models of the substructure usually using only surficial data. Although the velocity model is not over-resolved, the interpretations of it in the eyes of a geophysicist may be; whereas, a structural geologist may say that the models are much too simple for such a complicated, chaotic area. We try to bridge the gap between the two philosophies and provide seismically, petrologically, and bathymetrically constrained models addressing the mechanisms of exposing lower crustal and upper mantle rocks at the Hess Deep that were first discussed by *Francheteau et al.*, [1990].

Chapter 5

Topography Can Limit the Useful Range of Linearization in Tomographic Inversions

5.1 Abstract

Linearized inverse techniques are commonly used to solve for velocity models from travel time data. The amount models may change without violating the linearity assumption is dependent on the surface topography and parameterization. If, in a weak velocity gradient model, rays turn beneath a valley with topography similar to the radius of curvature of the ray paths, then large nonlinearities will result from small model perturbations. Hills, conversely, create environments in which the data are more linearly related to the models for the same model perturbation. In this chapter we present simple, one layer, laterally homogeneous, constant gradient models to study the effect of topography and parameterization on the linearity of the relationship between travel time change and velocity model change.

5.2 Introduction

During April-May 1992, a seismic refraction experiment was conducted across the Hess Deep rift valley in the eastern Pacific [Wiggins *et al.*, 1993]. Sea floor seismic measurements were made to constrain the shallow, 1-2 km, velocity structure in support of the Ocean Drilling Program's Leg 147. The Office of Naval Research-type ocean bottom seismometers [Sauter *et al.*, 1990] were used with explosive bottom shots [Dorman, 1993; Hammer *et al.*, 1994] to measure p-wave travel times through oceanic crust. The relationship between the travel time data and the velocity structure of the rock is not linear. The relationship was approximately linearized so that a

tomographic inversion procedure could be used iteratively to invert the data and solve for a velocity model. The main assumption in linearizing the relationship is that small perturbations in the model will produce proportionately small changes in the data. However, because an iterative approach is used, it is beneficial to take the largest step possible without violating the assumption of linearity. The unusually large topographic relief at the Hess Deep rift valley, more than 2 km elevation change in less than 8 km range, has demonstrated that the magnitude of allowable perturbation depends on the sea floor topography. In addition, the maximum linear step sizes are dependent on how the model is parameterized.

To invert the travel time data, the velocity model must be parameterized. The Hess Deep model is parameterized vertically as constant velocity gradient (dv/dz) layers. The layers were held at constant depths beneath the bathymetry producing a three-dimensional starting model with iso-velocity surfaces that followed the bathymetry. Horizontally, the layers are parameterized as a finite set of Fourier harmonics to impose a smoothing constraint. This parameterization scheme, along with the inverse procedures, were discussed by Hammer et al. [1994]. Their success with the Jasper Seamount seismic tomography experiment led us to employ the same techniques. A stable solution for the Jasper Seamount was obtained in one step with velocity perturbations up to ± 1 km/s. In the Hess Deep experiment, we are less fortunate with model perturbations of this magnitude, as some of the parameters stop changing after a few iterations, but many oscillate and will not converge to a stable solution.

The Hess Deep rift valley is a topographically complex area. The general area of our seismic refraction study consists of three main features: the valley of the Hess Deep, the hill or dome of the intra-rift ridge, and the incline from the valley up to the hill. The region of the model that corresponds to the oscillating parameters is the valley. The model oscillations initially have peak values of ± 300 m/s which diverge to

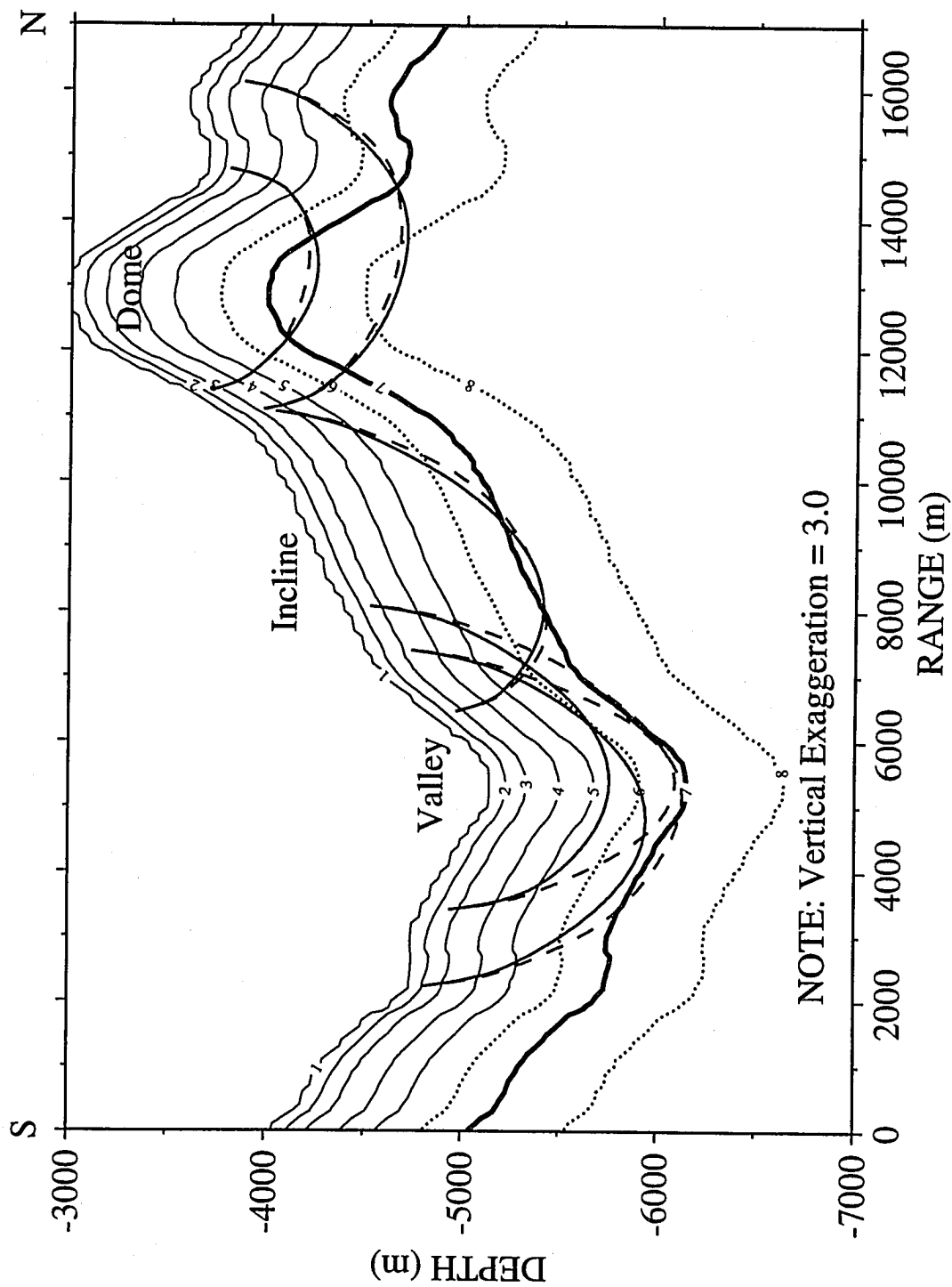
+/- 500 m/s after only 10 iterations. In contrast, the hill and incline regions converge to a stable solution within one relatively large step.

The large nonlinearity exhibited in the valley results from the ray paths moving from one layer of the model to another between iterations. As an example, a few ray paths for the west line of the refraction survey are shown with the two-dimensional cross section of the bathymetry (Figure 5.1). The contours that follow the bathymetry are the interfaces between the layers. The rays are traced in two "laterally" homogeneous models differing only by 300 m/s at the seventh interface. In this paper, "laterally" homogeneous means that at a given depth beneath the topography the velocity is the same, independent of range; thus, iso-velocity lines also follow the bathymetry. In the valley, there is a large change in the ray paths between the two models; whereas, the incline and hill regions show little change in the ray paths. The nonlinearity due to a change in one model parameter (layer velocity gradient) affecting the sampling of another parameter is small if the change in the ray path is small. However, this is not the case in the valley where a change in the model causes a large part of the rays' total path to go from sampling one layer to sampling another. Layer/parameter switching should be considered a catastrophic nonlinearity because the relationship between a datum and its sampled model parameters is greatly altered.

The solution to this problem is quite simple: take much smaller steps. This approach has been successfully applied to the Hess Deep data. Our modeling resolves anomalously high surficial velocities in the intra-rift ridge that are apparently due to a buoyant low velocity diapir approximately 2 km beneath the surface. We also resolve low velocities beneath the valley caused by rock fracturing at the tip of the Cocos-Nazca Spreading Center [Wiggins *et al.*, 1994]. The results correspond well with our initial study using the interactive ray tracing/model perturbing program, "MacRay" [Luetgert, 1992], as an independent method to produce one and two dimensional

velocity profiles of the Hess Deep area. With the use of smaller model perturbations, the movement of the rays in the valley is lessened and their transition between layers becomes smoother. However, even if the catastrophic nonlinearity is not present (i.e. rays do not drastically move in and out of layers), the valley still exhibits a higher level of nonlinearity than the incline or hill. The remainder of this paper addresses the factors contributing to this undesirable characteristic.

Figure 5.1 Two-dimensional cross section of the bathymetry at the Hess Deep, vertical exaggeration is 3. The contours that follow the bathymetry are interfaces between constant velocity gradient layers. The solid ray paths are traced through an average EPR crust, one-dimensional velocity profile reference model [Vera *et al.*, 1990]. The dashed ray paths are traced through a similar model differing by 300 m/s at the seventh interface. The models are different only between the dotted interfaces. Note the large change in ray paths in the valley compared to the dome.



5.3 Flat Laterally Homogeneous Earth

A flat Earth with no lateral heterogeneity is chosen as a familiar and simple model. The vertical is parameterized as a single layer with a constant gradient. If the problem is cast in velocity, then the gradient is dv/dz ; whereas, if depth is chosen as the dependent variable, then the reciprocal of the velocity gradient is used, dz/dv . If the velocity at the turning depth of a ray, $v_p = 1/p$ (where, p is the horizontal ray slowness), can be held constant and a much larger data set is used (e.g., multichannel seismic surveys), then parameterizing the model as dz/dv results in a completely linear relationship between data and model change. However, because of the relatively small amount of data and fixed source/receiver spacing, dv/dz was used to parameterize the layers of the Hess Deep model.

From the Eikonal equation it can be shown that travel time, T , and source/receiver spacing, X , are linearly related to the parameter dz/dv in a flat, one layer, laterally homogeneous Earth:

$$T = 2 \frac{dz}{dv} \ln \left[\frac{1}{p v_0} \left[1 + \left(1 - p^2 v_0^2 \right)^{1/2} \right] \right] \quad (5.1)$$

and

$$X = 2 v_p \frac{dz}{dv} \left[1 - \frac{v_0^2}{v_p^2} \right]^{1/2} \quad (5.2)$$

[*Garmany, 1978; Dorman 1979*]. Equation (5.1) is plotted in figure 5.2a as a dashed line for p held constant. While holding X constant, equation (5.2) is solved for v_p using different dz/dv models. v_p is then substituted back into equation (5.1) producing the solid curve of figure 5.2a. The first derivative or slope, $\frac{dT}{dm}$, is plotted in figure 5.2b and the second derivative, $\frac{d^2T}{dm^2}$, is plotted in figure 5.2c, both as functions of m .

The first derivative is a measure of the sensitivity of the data to changes in the model. A large magnitude of $\frac{dT}{dm}$ is desirable because large sensitivity equates to a small number of iterative steps. The second derivative is a measure of the change in sensitivity, or nonlinearity, of the relationship between data and model. In order to uphold the linearity assumption, large magnitudes of $\frac{d^2T}{dm^2}$ must be avoided. If p is held constant in equation (5.1), then the relationship is exactly linear as shown by the straight line, constant slope, and zero second derivative of figure 5.2. However, in the study of the Hess Deep, we hold the source/receiver spacing constant. For X held constant and small dz/dv (large velocity gradients), the magnitude of $\frac{d^2T}{dm^2}$ is large. Therefore, for a given model step size, the relationship between T and m is more linear for large m than for small m .

Because we cannot hold p constant and we do sample both weak and strong velocity gradient rock (lower and upper oceanic crust) at the Hess deep, there are no advantages in parameterizing our model as layers of constant reciprocal velocity gradients, dz/dv . The success of the Jasper Seamount study led us to use layers of constant velocity gradients, dv/dz , as parameterization for our model. The travel time curve from figure 5.2a, for X held constant, is transformed from dz/dv to dv/dz parameter space. The plots of T along with $\frac{dT}{dm}$ and $\frac{d^2T}{dm^2}$ versus dv/dz are shown in figure 5.3. Figure 5.3c shows that the relationship between T and m is nonlinear when m is small. In this case, however, small m corresponds to the weak velocity gradients seen in the lower crust; whereas, small dz/dv in the previous example corresponds to the strong velocity gradients seen in the upper crust. Therefore, whether a given model change violates the linearity assumption depends on both the parameterization and velocity gradient.

In both examples, the relationship between data and model is near-linear when the model parameter is large. However, dv/dz is a better choice for parameterization because at high values of m the sensitivity, $\frac{dT}{dm}$, is more than an order of magnitude larger than for dz/dv . In other words, if dz/dv is used, then larger changes in m are needed at large values of m (i.e. $m > 2$) to change the data by the same amount than if dv/dz is used. In addition, the change in sensitivity is less over m for dv/dz than for dz/dv (figures 5.2b & 5.3b). This explains why the nonlinear values for dz/dv (figure 5.2c) are larger at small m than for dv/dz (figure 5.3c).

Another way of describing the dependence of linear step size on the velocity gradient is by ray path differences between different models. Figure 5.4 is a plot of ray paths through four, constant velocity gradient, flat Earth models. There is a large difference between the ray path traced through the model with a constant velocity gradient of 0.25 sec^{-1} to one traced through a gradient of 2 sec^{-1} (i.e. step size of 1.75 sec^{-1}). In contrast, a model change of 4 sec^{-1} to 8 sec^{-1} produces a much smaller difference in ray paths. This shows rays are much more sensitive to model changes in weak velocity gradients than in strong gradients. Young eastern Pacific oceanic crust can be thought as consisting of two primary regions: the strong velocity gradient upper crust and the weak velocity gradient lower/middle crust. If the distance between the source and receiver is small, then the associated ray path will have a shallow turning point and only sample the upper crust. The lower crust can be sampled if the source/receiver spacing is sufficiently large. The Hess Deep experiment was designed to sample both primary regions of the crust. As in the flat Earth example above, we only had nonlinearity problems with rays turning in the weak velocity gradient region, deeper than 500 meters beneath the sea floor. However, this was true only of the rays traveling beneath the valley; the rays traced through the hill and incline were well-

behaved.

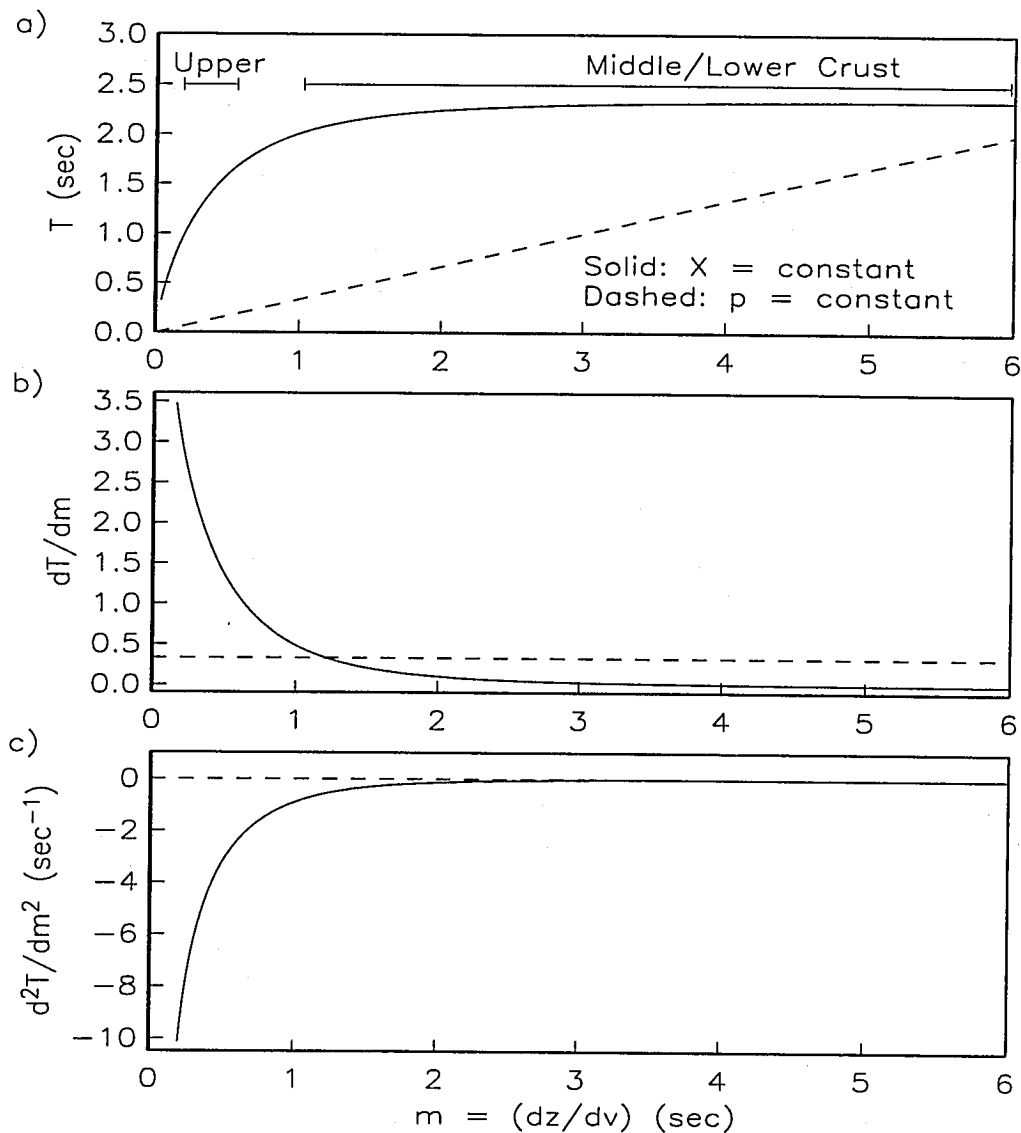


Figure 5.2 Analytical computations from equations (5.1) and (5.2) for a constant dz/dv gradient layer, flat Earth. If p is held constant (dashed lines) then the relationship between data and model is exactly linear. Constant source/receiver spacing, X , is the solid line. Small m corresponds to the upper oceanic crust (strong velocity gradients) and large m corresponds to the lower oceanic crust where weak velocity gradients prevail. a) Travel time, T , vs model parameter, m . b) The slope, $\frac{dT}{dm}$, vs m . Linearity is seen as a horizontal line. For X held constant and large m , the data are insensitive (small magnitude of $\frac{dT}{dm}$) to small model changes. c) The second derivative, $\frac{d^2T}{dm^2}$, vs m . A value of zero depicts linearity. For X held constant, approximate linearity is achieved with large dz/dv .

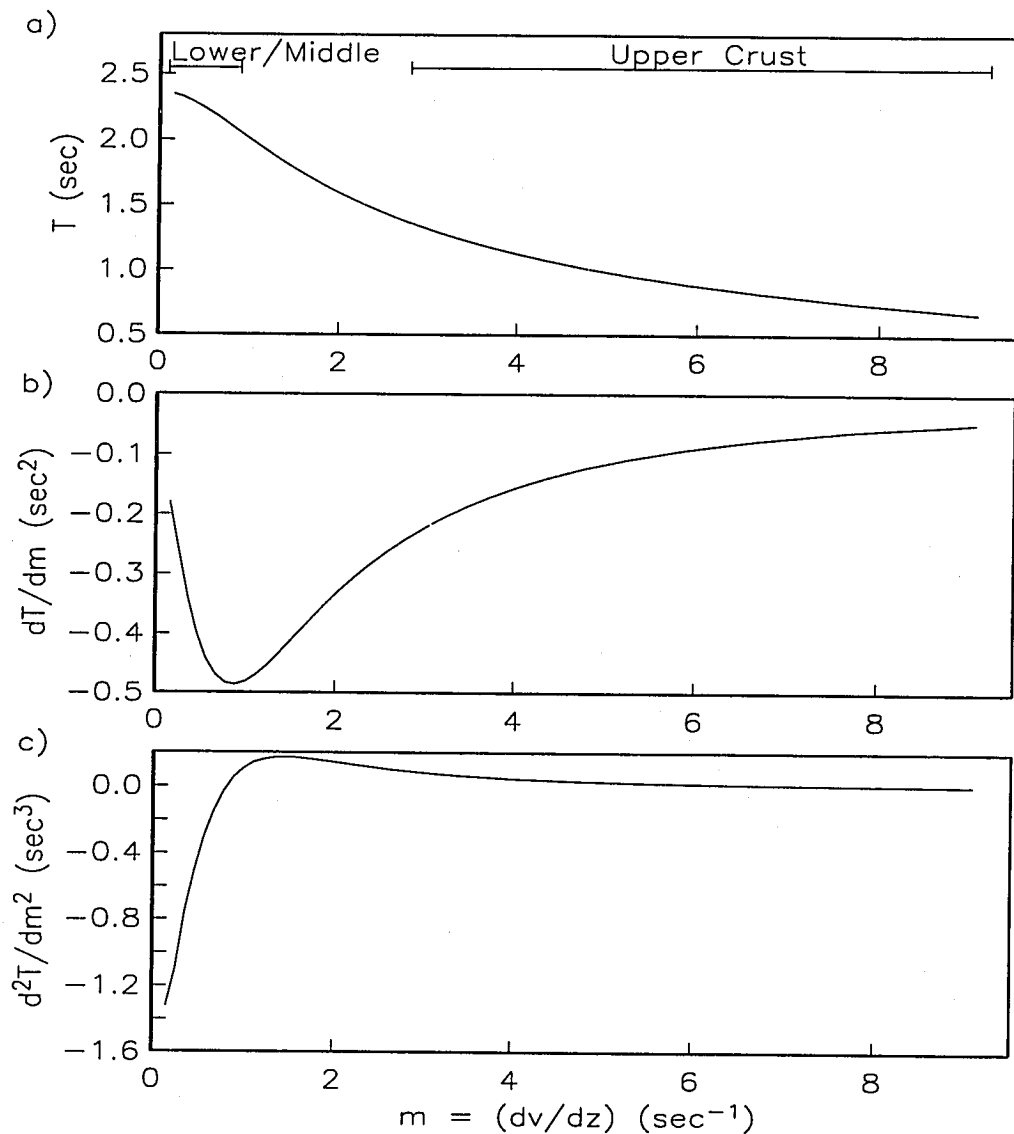


Figure 5.3 Analytical computations from equations (5.1) and (5.2) for a single, constant velocity gradient (dv/dz) layer, flat Earth. Only source/receiver spacing, X , held constant is shown because p held constant is not linear in dv/dz model parameter space. Small m corresponds to the lower oceanic crust (weak velocity gradients) and large m corresponds to the upper oceanic crust where strong velocity gradients prevail. a) Travel time, T , vs model parameter, m . b) The slope, $\frac{dT}{dm}$, vs m . Linearity would be seen as a horizontal line. c) The second derivative, $\frac{d^2T}{dm^2}$, vs m . A value of zero depicts linearity. For X held constant, approximate linearity is achieved with large dv/dz .

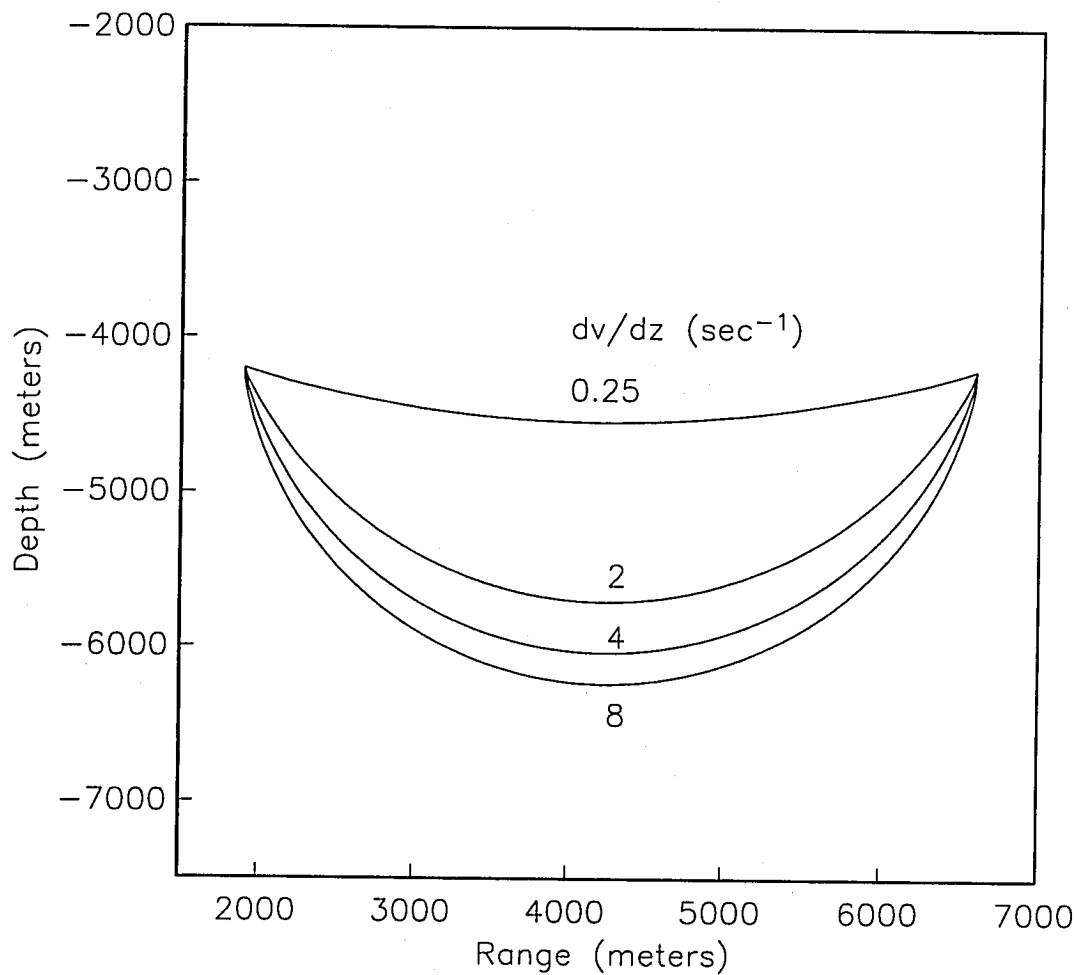
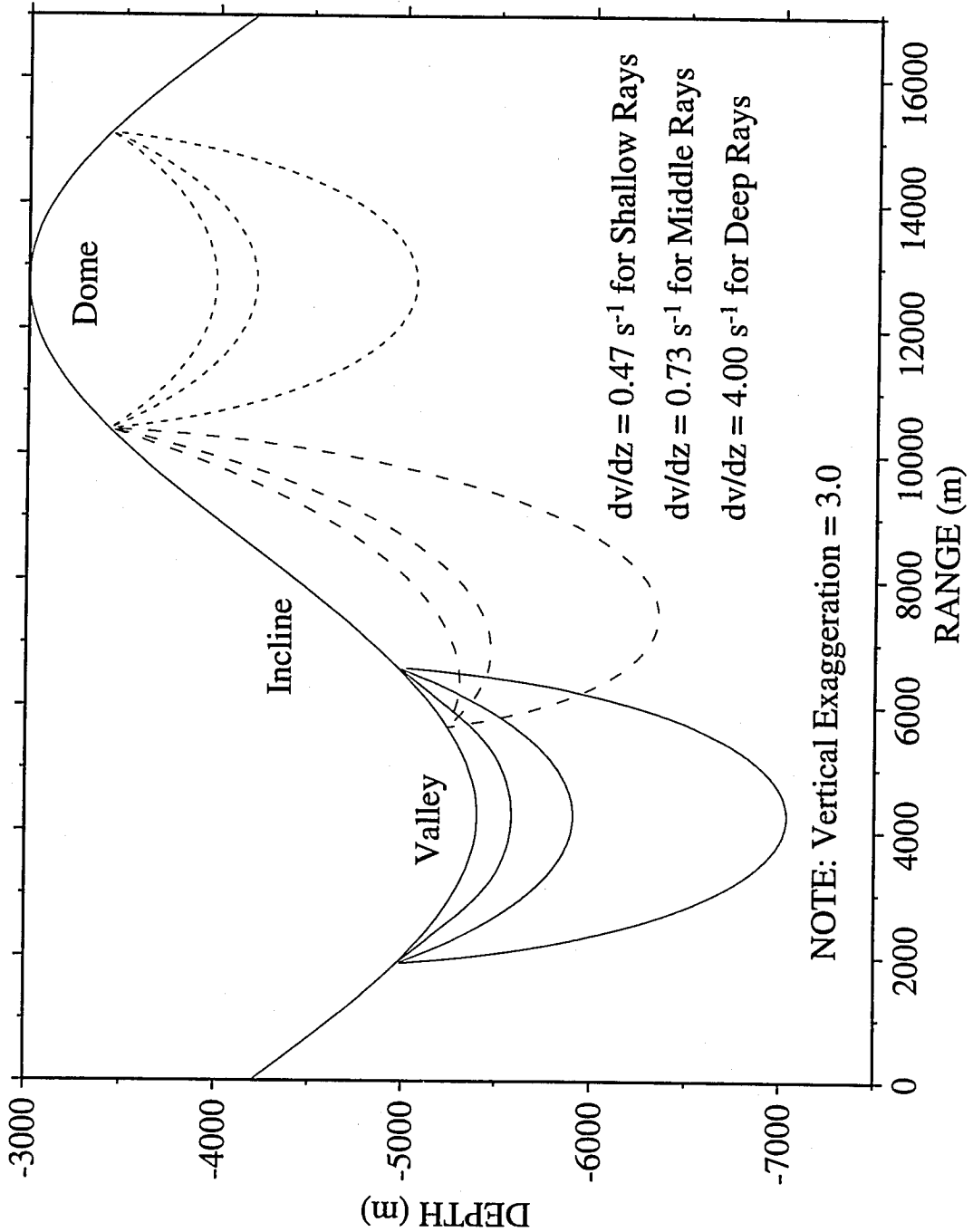


Figure 5.4 Ray paths traced through four, constant velocity gradient layer, flat Earth models. The difference in ray paths is much greater for a step of 1.75 sec^{-1} in a weak velocity gradient model than for a larger step of 4 sec^{-1} in a strong gradient. Ray paths are much more sensitive to model changes in weak velocity gradients.

5.4 Sinusoidal Topography Earth Model

To investigate the effect of topography on the linearity of the relationship between data and model, we introduce a single layer Earth model with a sinusoidal topography. The layer is parameterized as a constant velocity gradient with no "lateral" heterogeneity. The size and shape of the model were chosen to correspond to the dimensions of the Hess Deep model and to produce topographic curvature on the scale of the ray paths. Figure 5.5 is a plot of the topography as a function of range along with ray paths sampling three models of different velocity gradients in the three topographic regions of the model: valley, incline and dome. A comparison among the rays traced in the topographic regions reveals that the departure from the middle ray of the shallow and deep rays is greater in the valley than in the dome. This can be explained by the Earth-flattening approximation [e.g., *Aki & Richards*, 1980]; in which, a hill is approximated as a flat Earth with a stronger velocity gradient and a valley is approximated as a flat Earth with a weaker velocity gradient. When the ray path curvature is on the scale of the topography this approximation becomes important and can be understood geometrically. The change in direction of the ray's path is related to the direction of the velocity gradient. Because the velocity gradient is perpendicular to the topography, a ray traveling in the valley spends a greater part of its path near-perpendicular to the gradient, as do rays in weak velocity gradient medium. Conversely, a ray traveling in the hill spends a larger portion of its path near-parallel to the direction of the velocity gradient, as do rays in strong gradient environments. In addition, valleys are inherently weak gradient regions caused by talus accumulation at the base of hills and/or intense cracking of the rifted crust. It should be clear from the previous discussion of the dependence of ray paths on models of different velocity gradients (figure 5.4) that the effective weaker velocity gradient in the valley causes the rays there to be more sensitive to model changes.

Figure 5.5 Two-dimensional cross section of the sinusoidal topography model with a constant velocity gradient layer, vertical exaggeration is 3.0. The size and shape of the model were chosen to correspond to the dimensions of the Hess Deep model. Rays are traced for models of different velocity gradients in the three topographic regions: valley (solid rays), incline (large dashed rays) and dome (small dashed rays). A comparison among the rays traced in the topographic regions reveals that the departure from the middle ray of the shallow and deep rays is greater in the valley than in the dome. This is because valleys decrease the effective velocity gradient; whereas, hills increase the effective gradient.



The travel time curves in figures 5.2a and 5.3a were produced analytically from equations (5.1) and (5.2) and were verified by tracing rays through corresponding flat Earth models. Because analytical expressions do not exist for non-flat Earth models, the travel time versus velocity gradient curves must be produced by tracing rays through the sinusoidal topography models. Figure 5.6 shows T , $\frac{dT}{dm}$, and $\frac{d^2T}{dm^2}$ versus model parameter, $m = dv/dz$, for the three regions of figure 5.5. The solid curves correspond to the valley, the large dashed curves are for the incline, and the small dashed curves are for the dome. The effect of topography can be seen in the displacement of the curves along the abscissa. The valley moves the $\frac{d^2T}{dm^2}$ curve to the right, causing nonlinear effects to be important in a stronger gradient region; whereas, the dome moves the curve to the left allowing weaker velocity gradients to be used without violating the linearity assumption (figure 5.6c). As an example, if the velocity gradient is 0.5 sec^{-1} through out the model, figure 5.6c shows that the valley exhibits a higher level of nonlinearity ($\frac{d^2T}{dm^2}$) than the dome. Thus, the valley topography effectively lowers the velocity gradient, making deep turning rays behave more nonlinearly to model changes.

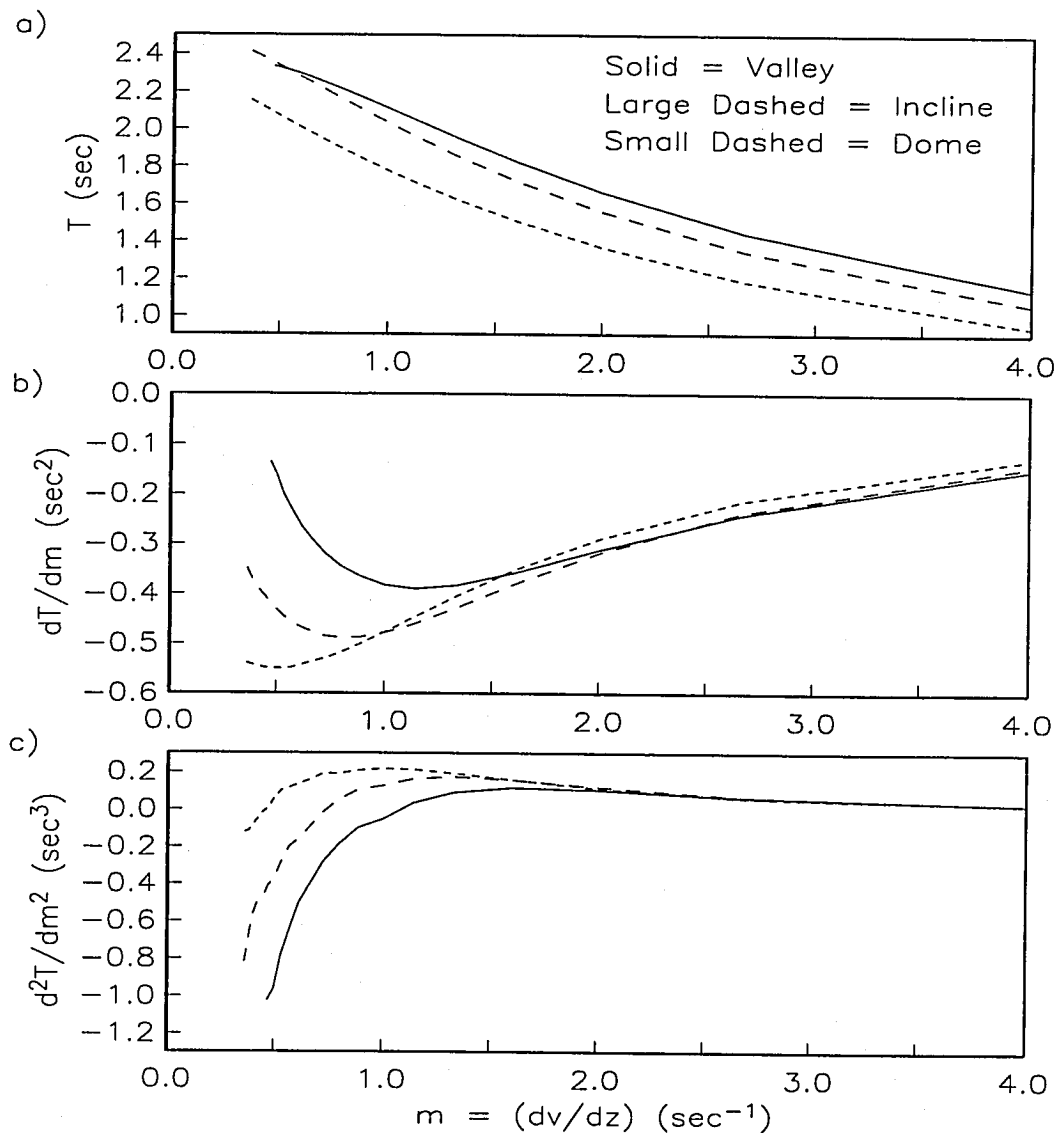


Figure 5.6 Data/model relationship plots for a constant velocity gradient layer, sinusoidal topography model for rays traced in the three topographic regions: valley (solid curves), incline (large dashed curves), and dome (small dashed curves). a) Travel time, T , vs model parameter, m . b) The slope, $\frac{dT}{dm}$, vs m . Linearity would be seen as a horizontal line. c) The second derivative, $\frac{d^2T}{dm^2}$, vs m . A value of zero depicts linearity. The displacement of the solid curve to the right shows the valley effectively lowers the velocity gradient, producing higher nonlinearities than the hill (small dashed curve displaced to the left).

5.5 Conclusion

It is important to understand the limitations of linearization when conducting a linear tomographic inverse. In seismic refraction modeling, the behavior of the ray paths limits the allowable linear velocity perturbation. How the model is parameterized, where the ray travels in the model, and the topography are all factors contributing to the nonlinear behavior of ray paths.

If, under ideal conditions, large amounts of data are used and p is held constant, then the model should be parameterized as dz/dv because the relationship between data and model is exactly linear. However, holding X constant with this model parameter will yield large nonlinearities in a strong velocity gradient region (small m) such as that of the upper oceanic crust. For a given step size, the travel time of the rays turning in the lower crust (large m) are more linearly related to model changes (small $\frac{d^2T}{dm^2}$), but also less sensitive (small $\frac{dT}{dm}$). Using dv/dz as the model parameter results in greater sensitivity of the data to model changes for large m , as well as smaller nonlinearity values over all of m . However, the general characteristics of the maximum linear step size of the upper and lower crustal regions for dv/dz are opposite of the dz/dv parameterization.

Topography affects the nonlinearity of the data/model relationship via the Earth-flattening approximation. A valley effectively weakens the velocity gradient of the region causing large nonlinearities in the already weak gradient area of the lower crust. Conversely, a hill effectively increases the velocity gradient which decreases the nonlinearity as seen in the movement of the $\frac{d^2T}{dm^2}$ versus m curve to the left. It is now clear why Hammer et al. [1994] were able to take such large steps with the Jasper Seamount dome-like model and we could not in the Hess Deep rift valley. For deep

(weak velocity gradient) turning rays traveling beneath a valley, it is necessary to make very small velocity model perturbations to keep the relationship between the data and model near-linear.

REFERENCES

- Aki, K. and Richards, P. G., *Quantitative Seismology Theory and Methods*, vol. I & II, W. H. Freeman, San Francisco, 1980.
- Cornuelle, B., Munk, W., and Worcester, P., Ocean Acoustic Tomography from Ships, *J. Geophys. Res.*, *94*, 6232-6250, 1989.
- Creager, K. C. and Dorman, L. M., Location of Instruments on the Seafloor by Joint Adjustment of Instrument and Ship Positions, *J. Geophys. Res.*, *87*, 8379-8388, 1982.
- Dick, H. J. B., Gillis, K., Lonsdale, P., and Natland, J., Deep Crustal Drilling in Fast-Spread Crust Exposed at the Hess Deep, *Drilling proposal submitted to ODP*, 1990.
- Dorman, LeRoy M., A linear relationship between Earth models and seismic body wave data, *Geophys. Res. Lett.*, *6*, 132-134, 1979.
- Dorman, LeRoy M., The Low-frequency Seismic Moment of Deep Underwater Explosions, *Eos*, *74*, 396, 1993.
- Francheteau, J., Armijo, R., Cheminee, J. L., Hekinian, R., Lonsdale, P., and Blum, N., 1 Ma East Pacific Rise oceanic crust and uppermost mantle exposed by rifting in Hess Deep (equatorial Pacific Ocean), *Earth Planet. Sci. Lett.*, *101*, 281-295, 1990.
- Francheteau, J., Armijo, R., Cheminee, J. L., Hekinian, R., Lonsdale, P., and Blum, N., Dyke complex of the East Pacific Rise exposed in the walls of Hess Deep and the structure of the upper oceanic crust, *Earth Planet. Sci. Lett.*, *111*, 109-121, 1992.
- Franklin, Joel N., Well-Posed Stochastic Extensions of Ill-Posed Linear Problems, *Journal of Mathematical Analysis and Applications*, *31*, 682-716, 1970.
- Garmany, J. D., *Methods of seismic travel time calculation and inversion and of synthesizing high frequency seismograms: Ph. D. thesis*, University of California, San Diego, 1978.
- Gillis, K., Mevel, C., Allan, J., and , et al., Initial Reports, *Proceedings of the Ocean Drilling Program*, *147*, 1993.
- Hammer, P. T. C., Dorman, L. M., Hildebrand, J. A., and Cornuelle, B. D., Jasper Seamount Structure: Seafloor Seismic Refraction Tomography, *J. Geophys. Res.*, *99*, 6731-6752, 1994.

- Hey, R. N., Deffeyes, K. S., Johnson, G. L., and Lowrie, A., The Galapagos Triple Junction and Plate Motions in the East Pacific, *Nature*, 237, 20-22, 1972.
- Hey, R. N., Kleinrock, M. C., Miller, S. P., Atwater, T. M., and Searle, R. C., Sea Beam/Deep Tow Investigation of an Active Oceanic Propagating Rift System, Galapagos 95.5 deg. W, *J. Geophys. Res.*, 91, 3369-3393, 1986.
- JOIDES,, Leg 147 Prospectus: Hess Deep, *Joint Ocean. Inst. Deep Earth Sampling J.*, 18, 12-15, no. 3, 1992.
- Kashintsev, G. L., Kuzmin, M. I., and Poplitov, E. N., Composition and structure of the oceanic crust in the vicinity of the Hess Basin (Pacific Ocean), *Geotectonics*, 16, 512-520, 1982.
- Lonsdale, P., Regional Shape and Tectonics of the Equatorial East Pacific Rise, *Mar. Geophys. Res.*, 3, 295-315, 1977.
- Lonsdale, P., Linear Volcanoes along the Pacific-Cocos Plate Boundary, 9° N to the Galapagos Triple Junction, *Tectonophysics*, 116, 255-279, 1985.
- Lonsdale, P., Blum, N., and Puchelt, H., The RRR triple junction at the southern end of the Pacific-Cocos East Pacific Rise, *Earth Planet. Sci. Lett.*, 109, 73-85, 1992.
- Lonsdale, P. F., Structural Pattern of the Galapagos Microplate and Evolution of the Galapagos Triple Junctions, *J. Geophys. Res.*, 93, 13551-13574, 1988.
- Luetgert, J., Interactive Two-Dimensional Seismic Raytracing for the Macintosh, *U.S. Geological Survey Open File Report 92-356*, 1992.
- MacLeod, C. J., Celerier, B., Harvey, P. K., and Party, ODP Leg 147 Scientific, Further techniques for core reorientation by Core-log integration: Applications to structural studies of the lower oceanic crust in Hess Deep, Eastern Pacific, *Geological Applications of Borehole Wall Imaging*, Spec. Publ. Geol. Soc. London, in press.
- McKenzie, D. P. and Morgan, W. J., Evolution of Triple Junctions, *Nature*, 224, 125-133, 1969.
- Neprochnov, Yu. P., Sedov, V. V., Semenov, G. A., Yel'nikov, I. N., and Filaktov, V. D., The Crustal Structure and Seismicity of the Hess Basin Area in the Pacific Ocean, *Oceanology*, 20, 317-322, 1980.
- Raff, A. D., Sea Floor Spreading: Another Rift, *J. Geophys. Res.*, 73, 3699-3705, 1968.

- Rudnik, G. B., Magmatic and metamorphic rocks in Hess Deep (in Russian), *Geological-Geophysical Researches in the Southeastern Part of the Pacific Ocean*, 116-125, Nauka, Moscow, 1976.
- Sauter, A. W., Hallinan, J., Currier, R., Barash, T., Wooding, B., Schultz, A., and Dorman, L. M., A New Ocean Bottom Seismometer, *Proceedings of Conference: Marine Instrumentation '90*, 99-104, Marine Technology Society, 1990.
- Searle, R. C. and Hey, R. N., GLORIA Observations of the Propagating Rift at 95.5° W on the Cocos-Nazca Spreading Center, *J. Geophys. Res.*, 88, 6433-6447, 1983.
- Searle, R. C. and Francheteau, J., Morphology and Tectonics of the Galapagos Triple Junction, *Mar. Geophys. Res.*, 8, 95-129, 1986.
- Toomey, D. R., Solomon, S. C., and , G. M. Purdy, Tomographic Imaging of the Shallow Crustal Structure of the East Pacific Rise at 9 deg 30 min N , *J. Geophys. Res.*, 99, 24135-24157 , 1994.
- Vera, E. E., Mutter, J. C., Buhl, P., Orcutt, J. A., Harding, A. J., Kappus, M. E., Detrick, R. S., and Brocher, T. M., The Structure of 0- to 0.2-m.y.-old Oceanic Crust at 9° N on the East Pacific Rise from Expanded Spread Profiles, *J. Geophys. Res.*, 95, 15529-15556, 1990.
- Wernicke, B., Uniform-sense normal simple shear of the continental lithosphere, *Can. J. Earth Sci.*, 22, 108-125, 1985.
- Wiggins, Sean M., Canuteson, Eric L., Dorman, LeRoy M., Hildebrand, John A., Sauter, Allan W., and Schreiner, Anthony E., Crustal Structure at the Hess Deep: Seismic Studies Show High Velocity and Density in the Intra-rift Ridge , *Eos*, 73, 356, 1992.
- Wiggins, Sean M., Canuteson, Eric L., Dorman, LeRoy M., Hildebrand, John A., Cornuelle, Bruce D., Sauter, Allan W., and Schreiner, Anthony E., Crustal Structure at the Hess Deep: Seismic Studies Show High Velocity in the Intra-rift Ridge and Low Velocity in the Deep, *Eos*, 74, 666, 1993.
- Wiggins, Sean M., Dorman, LeRoy M., and Cornuelle, Bruce D., Linearization Limitations of Tomographic Inversion Due to Topography , *Eos*, 75, 444 , 1994.
- Zonenshain, L. P., Kogan, L. I., Savostin, L. A., Golmstock, A. Ja., and Gorodnitskii, A. M., Tectonics, Crustal Structure and Evolution of the Galapagos Triple Junction, *Marine Geology*, 37, 209-230, 1980.